Tracking small-scale tropical forest disturbances: fusing the Landsat and Sentinel-2 data record

Yihang Zhang [1], Feng Ling [1, 2*], Xia Wang [3], Giles M. Foody [4], Doreen S. Boyd [4], Xiaodong Li [1], Yun Du [1], and Peter M. Atkinson [5,6,7]

1. Key Laboratory of Monitoring and Estimate for Environment and Disaster of Hubei province, Innovation Academy for Precision Measurement Science and Technology, Chinese Academy of Sciences, Wuhan 430077, China;
2. Sino-Africa Joint Research Centre, Chinese Academy of Sciences, Wuhan 430074, China;
3. Research Center for Environmental Ecology and Engineering, School of Environmental Ecology and Biological Engineering, Wuhan Institute of Technology, Wuhan 430205, China;
4. School of Geography, University of Nottingham, NG7 2RD Nottingham, UK;
5. Lancaster Environment Center, Faculty of Science and Technology, Lancaster University, Lancaster LA1 4YQ, UK;
6. School of Geography and Environmental Science, University of Southampton, Highfield, Southampton SO17 1BJ, UK;
7. Institute of Geographic Sciences and Natural Resources Research, Chinese Academy of Sciences, 11A Datun Road, Beijing 100101, China.

([*]Corresponding authors: Feng Ling. E-mails: lingf@whigg.ac.cn, zhangyihang@apm.ac.cn)

Abstract: Information on forest disturbance is crucial for tropical forest management and global carbon cycle analysis. The long-term collection of data from the Landsat missions provides some of the most valuable information for understanding the processes of global tropical forest disturbance. However, there are substantial uncertainties in the estimation of non-mechanized, small-scale (i.e., small area) clearings in tropical forests with Landsat series images. Because the appearance of small-scale openings in a tropical tree canopy are often ephemeral due to fast-growing vegetation, and because clouds are frequent in tropical regions, it is challenging for Landsat images to capture the logging signal. Moreover, the spatial resolution of Landsat images is typically too coarse to represent spatial details about small-scale clearings. In this paper, by fusing all available Landsat and Sentinel-2 images, we proposed a method to improve the tracking of small-scale tropical forest disturbance history with both fine spatial and temporal resolutions. First, yearly composited Landsat and Sentinel-2 self-referenced normalized burn ratio (*r*NBR) vegetation index images were calculated from all available Landsat-7/8 and Sentinel-2 scenes during 2016-2019. Second, a deep-learning based downscaling method was used to predict fine resolution (10 m) *r*NBR images from the annual coarse resolution (30 m) Landsat *r*NBR images. Third, given the baseline Landsat forest map in 2015, the generated fine-resolution Landsat *r*NBR images and

original Sentinel-2 *r*NBR images were fused to produce the 10 m forest disturbance map for the period 2016-2019. From data comparison and evaluation, it was demonstrated that the deep-learning based downscaling method can produce fine-resolution Landsat *r*NBR images and forest disturbance maps that contain substantial spatial detail. In addition, by fusing downscaled fine-resolution Landsat *r*NBR images and original Sentinel-2 *r*NBR images, it was possible to produce state-of-the-art forest disturbance maps with OA values more than 87% and 96% for the small and large study areas, and detected 11% to 21% more disturbed areas than either the Sentinel-2 or Landsat-7/8 time-series alone. We found that 1.42% of the disturbed areas indentified during 2016-2019 experienced multiple forest disturbances. The method has great potential to enhance work undertaken in relation to major policies such as the reducing emissions from deforestation and forest degradation (REDD+) programmes.

Keywords: Forest disturbance, small-scale clearing, Landsat and Sentinel-2, deep learning, downscaling.

1. Introduction

Tropical forests hold 471 ± 93 Pg of carbon, more than the total carbon stored in all other forests on the planet and, therefore, play a major role in key environmental challenges such as climate change and the provision of ecosystem services (Pan et al. 2011; Baccini et al. 2017). Disturbance of these forests via deforestation and degradation impacts greatly on forest ecosystem structure and function (Uriarte et al. 2009), because it unlocks stored carbon via gaseous emissions into the atmosphere at significant levels (Saatchi et al. 2011). The Reducing Emissions from Deforestation and forest Degradation (REDD+) programme was initiated to mitigate global climate change resulting from greenhouse gas net emissions. The main objective of REDD+ is to enhance forest management in developing countries, which are host to the majority of the world's tropical forests. In support of REDD+ activities, it is crucial to provide information on where and when forest disturbance events occur. Satellite remote sensing has the potential to provide such information (Frolking et al. 2009; Dong et al. 2012b; Banskota et al. 2014; Hermosilla et al. 2016; Qin et al. 2019; Zhang et al. 2019).

Imagery from the Landsat series of satellites has been the primary data source for monitoring forest disturbance notably because of its moderate spatial resolution (30-80 m) and continuous acqusition since 1972 (Zhu et al. 2012; Banskota et al. 2014; Hermosilla et al. 2015), with numerous algorithms developed for use with it (Lu et al. 2004; Kennedy et al. 2007; Kennedy et al. 2010; Townshend et al. 2012; Bullock et al. 2020). These methods fall broadly into two categories, as determined by the temporal intensity of

64 the Landsat images used. One category uses Landsat images acquired at two or more times, from which
65 the disturbance may be assessed by using approaches such as post-classification analyses. Such studies
66 have used a range of methods including supervised/unsupervised classification (Cohen et al. 2002; Huang
67 et al. 2007; Dong et al. 2012a; Potapov et al. 2012), spectral unmixing (Souza et al. 2005; Asner et al.
68 2009), regression tree (Sexton et al. 2013), and spectral change analysis (Masek et al. 2008) to map of
69 forest cover, with the occurrence, location, and timing of disturbance events determined using difference
70 analysis. The second category uses time-series fitting methods to take advantage of the temporal
71 information in the potentially dense sequence of Landsat observations. Examples include vegetation
72 change tracker (VCT) (Huang et al. 2010), LandTrendr (Kennedy et al. 2010), Composites2Change (C2C)
73 (Hermosilla et al. 2016; White et al. 2017), and continuous monitoring of forest disturbance algorithm
74 (CMFDA) (Zhu et al. 2012). The multitemporal forest disturbance mapping approach can also be applied
75 to a dense series of images by dividing it into a sequence of image pairs. Such a strategy was, for example,
76 used with the global forest cover change (GFCC) products published by Hansen et al. (2013) to update
77 global annual forest cover loss since 2000. Critically, the two categories of forest disturbance mapping
78 approaches enable the assesment and monitoring of major forest disturbances such as those associated
79 with fire, urbanization, and mechanized agriculture.

80 Although the potential of satellite remote sensing as a source of information on forest disturbance
81 is well established, there remain some challenges that currently limit its application. In particular,
82 estimation of forest loss or degradation is often limited by issues such as cloud cover and rapid vegetation
83 regrowth, as well as an inability to study very small areas such as those associated with processes of
84 selective logging and smallholder clearing across tropical forests (Kalamandeen et al. 2018; Tyukavina
85 et al. 2018; Kleinschroth et al. 2019). Very small area forest disturbances are difficult to detect because
86 not only is the probability of obtaining a cloud-free image low, but also the small openings, often less
87 than 1 ha in size, may not be readily detectable and may be relatively ephemeral due to rapid regrowth
88 in the months after formation (Kleinschroth et al. 2016). Consequently, the logging signal (e.g., from
89 forest to bare soil) may become less detectable, gradually disappearing from the satellite record as
90 vegetation regrows. Yet, detecting these small-scale disturbances is important, not only for REDD+
91 purposes, but for other reasons such as monioring species turnover (Barlow et al. 2016) and human rights
92 violations (Jackson et al. 2020).

93 Generally, the coupled impact of frequent cloud cover and rapid forest regrowth can be overcome

using temporally dense image stacks. However, this is often impossible in tropical areas, especially in areas such as the Congo Basin, as only a small proportion of the imagery will be cloud-free. The limited cloud-free data available is often unable to detect all disturbance events before forest regrowth (Zhang et al. 2005; Ju and Roy 2008; Verbesselt et al. 2012; Tang et al. 2019). On the other hand, the detection of small canopy openings in tropical forests requires satellite sensor images with a spatial resolution that is fine enough to capture the landscape variability and critically is at a spatial scale that relates well to the scale of disturbance process affecting the forest (Hirschmugl et al. 2017). The spatial resolution of Landsat sensor imagery is too coarse to measure reliably subtle disturbances in the tropical forest canopy associated with small area logging activities. This is because the extent of the logged area may be smaller than a pixel, and even if larger than a pixel many of the boundary pixels may be of mixed composition (Souza et al. 2013). For example, the average width of logging roads caused by selective logging in the rainforest is ~7 m (Kleinschroth et al. 2019). Imagery with finer spatial and temporal resolutions than those offered by Landsat sensors is, therefore, required for monitoring tropical forest disturbances. The Sentinel-2A and Sentinel-2B satellites launched in June 2015 and March 2017, respectively, provide freely available multispectral imagery. Sentinel-2 images have a spatial resolution of, in some wavebands, 10 m and offer a joint revisit time frequency of five days, which is an improvement over the Landsat images for monitoring tropical forest disturbance (Vaglio Laurin et al. 2016; Lima et al. 2019). But the cloud cover is so persistent that even the 5-day revisit period offered by Sentinel-2 is in sufficient for the study of small scale forest disturbances.

While imagery from the Sentinel-2 satellite sensors may represent an improvement on Landsat sensor imagery for disturbance monitoring, there could be considerable advantage gained from their combined use. In particular, the use of both Sentinel-2 and Landsat sensor imagery would increase the probability of obtaining cloud-free imagery. The potential of the combined use of Sentinel and Landsat sensor images has been recognised and NASA has published a surface reflectance product by harmonizing Sentinel-2 and Landsat images (Claverie et al. 2018). These latter data are, however, provided at the Landsat spatial resolution which is too coarse for the detection of small disturbances such as those arising from very localised selective logging. It would be preferable to instead change the spatial resolution of Landsat images to that of Sentinel-2 and hence help address the problems associated with the relatively coarse spatial resolution of Landsat (Wang et al. 2017; Pouliot et al. 2018). According to the principles and methods of scaling geospatial data presented by Ge et al. (2019), increasing the spatial

resolution of Landsat images to that of Sentinel-2 is a geospatial data downscaling process, and the Sentinel-2 data could be used as the fine-scale auxiliary information to further increase the accuracy of downscaling the Landsat data.

In this paper, we propose a method to monitor small tropical forest disturbance events by fusing all available Sentinel-2 and Landsat-7/8 images acquired 2016-2019 with a deep learning approach. Our method exploits the fine temporal resolution image stack provided by the combination of Sentinel-2 and Landsat acquisition with the finer spatial resolution of the Sentinel-2 data. Instead of fusing directly the images acquired by the Sentinel and Landsat sensors, the modified normalized burn ratio (NBR) vegetation index is used for tracking forest disturbances. This is because the NBR index is effective in highlighting subtle changes in tropical forests (Langner et al. 2018). Specifically, yearly composited Landsat and Sentinel-2 self-referencing NBR (*r*NBR) vegetation index images were calculated from all available Landsat-7/8 and Sentinel-2 scenes during 2016-2019. A deep-learning approach for super-resolution (Kim et al. 2016a; Wang et al. 2020), based on a very deep convolutional network, was used to predict fine resolution (10 m) *r*NBR images from the coarse resolution (30 m) Landsat *r*NBR images by using the Sentinel-2 *r*NBR images as a training dataset. With the baseline of published global Landsat tree canopy cover map in 2015 (Sexton et al. 2013), the generated 10 m annual Landsat and original Sentinel-2 *r*NBR images were then fused to produce the final 10 m forest disturbance map for 2016-2019.

2. Study area and data sources

The study area in this paper is located in the northern rainforest of the Democratic Republic of the Congo (DRC) (Figure 1). The Congo Basin is known as one of the largest gene banks on the planet and hosts the world's second-largest tropical rainforest after the Amazon Basin. The DRC is, by area, the largest country in the Congo Basin, and includes both Africa's largest rainforest, and most of the Congo rainforests. However, due to the demands of agriculture, infrastructure, mining, and wood fuel, the DRC experienced an estimated average loss of 570,000 ha of rainforest per year from 2000 to 2014 (Harris et al. 2017). According to the classification map that indicated the drivers of global forest loss (Curtis et al. 2018), the forest loss in this study area is caused mainly by shifting agriculture. More precisely, smallholder clearings for agriculture, in which the forest logged area is often less than 1ha, has resulted in the main forest loss in the Congo tropical forest in recent decades (Tyukavina et al. 2018). In the DRC, 92.2% of forest loss during 2000-2014 was caused by non-mechanized small area clearing for agriculture,

and the logged wood taken from the rainforest was used mostly for wood fuel to support the DRC a population that is typically in severe poverty and with limited national energy infrastructure (Tyukavina et al. 2018). Given the abundance of small area forest logging and high frequency of cloud cover, the DRC is well-suited as a study area to validate the proposed method.

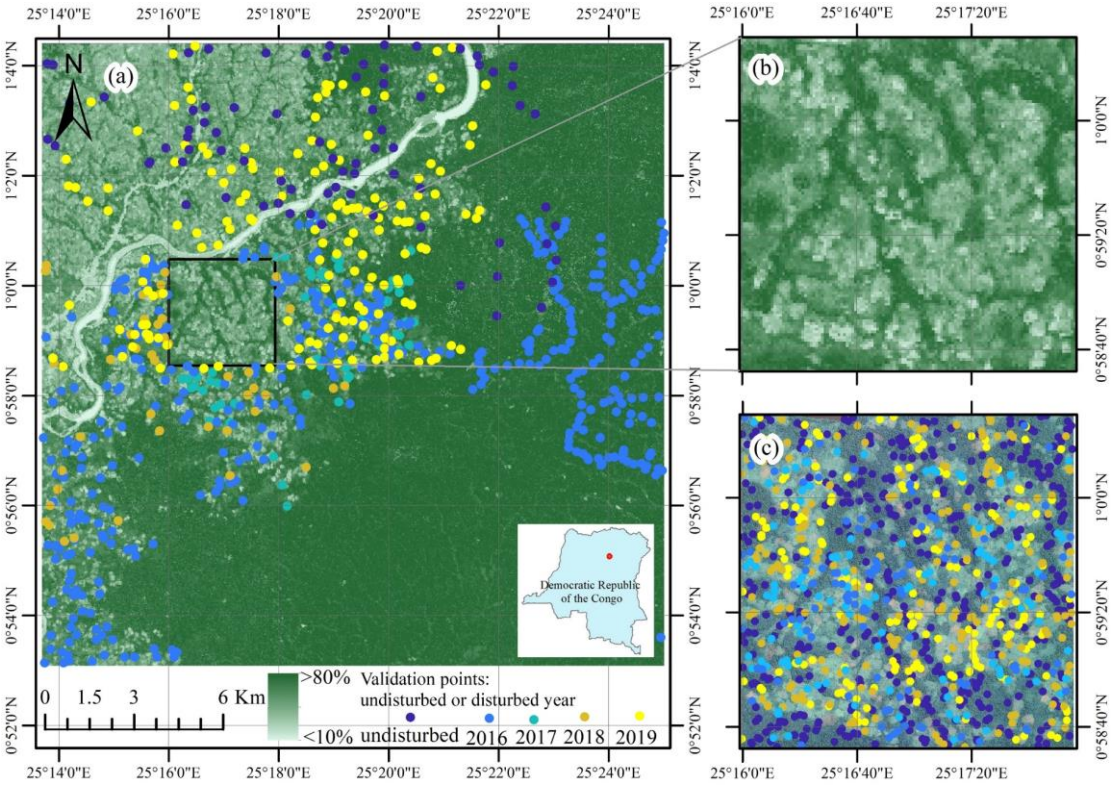

Figure 1. Study areas and data sets. (a) Landsat tree canopy cover map in 2015 and validation points covering the full, large study area in DRC; (b) Subset, small study area; (c) Validation points used in the subset, small study area (where dark blue means undisturbed point, and light blue, teal, orange, and yellow mean points disturbed in 2016, 2017, 2018 and 2019 respectively).

Table 1. The number of Landsat-7 ETM+, Landsat-8 OLI and Sentinel-2 MSI scenes used in this research.

Year	Landsat-7 ETM+	Landsat-8 OLI	Landsat-7&8	Sentinel-2 MSI
2016	15	17	32	61
2017	12	21	33	52
2018	9	17	26	70
2019	10	14	24	70
Total	46	69	115	253

As listed in Table 1, the ortho-rectified top-of-the-atmosphere (TOA) products available in the Google Earth Engine (GEE) cloud computing platform, including 46 scenes of Landsat-7 Enhanced Thematic Mapper (ETM+), 69 scenes of Landsat-8 Operational Land Imager (OLI), and 253 scenes of Sentinel-2 Multispectral Imager (MSI) from Jan. 2016 to Dec. 2019, are used in this research. Instead of

using the surface reflectance (SR) products in GEE, the above Landsat TOA products were chosen. This is because the cloud masking algorithms are designed only for the Landsat TOA products in GEE; moreover, as the NBR vegetation index is used to detect forest disturbances, there would be almost no difference in the NBR value calculated with the TOA and SR products. Note that from these data, it is evident that, there will be a Landsat or Sentinel-2 sensor image available every four days during the study period. The quality flag bands of the Landsat-7/8 and Sentinel-2 TOA products in GEE are first applied to detect clouds, and then the improved 'Fmask' algorithm (Qiu et al. 2019) is used to derive an additional quality band to further refine the detection of clouds and cloud-shadows. Additionally, a 500 m buffer is used to remove possible cloud edges or remnants that had not been masked properly by using the quality flag bands and 'Fmask' algorithm, and scene edges affected by sensor artifacts. The Landsat tree canopy cover (TCC) product (Sexton et al. 2013) estimated from the cloud-free annual growing season composite Landsat-7 ETM+ TOA data of circa 2015 is also used. Each pixel in the Landsat TCC product has a spatial resolution of 30 m and is encoded as a percentage per output grid cell, in the range 0–100. It is used to produce the baseline forest cover map in 2015, which is defined as the canopy cover >30% and vegetation taller than 5 m in height (Kim et al. 2014).

To validate the results produced by the proposed method, validation points are selected separately for the full, large study area (see Figure 1(a)) and the subset, small study area (see Figure 1(c)). In the small study area, annual subset Google Earth very high resolution (VHR, e.g., 2 m) images during 2015-2019 are used to identify the validation points, with 988 randomly selected validation points finally selected (see Figure 1(c)). For each of the validation points in the subset, small study area, the objective is to determine the disturbance type: undisturbed, or disturbed. If defined as an undisturbed point, no forest disturbance event occurred during 2016-2019; otherwise, if defined as a disturbed point, forest disturbance occurred in any year of 2016-2019. To obtain an accurate disturbance type for each validation point, the determination of the disturbance type of each validation point is based on the time-series VHR images, where the VHR image in 2015 is used together with the VHR image in 2016 to determine the disturbed points in 2016. For example, for a randomly selected validation point, a disturbed point in 2016, would be one covered by forests in the VHR image of 2015, for which the forests were logged in the VHR image of 2016. For a disturbed area, a process of vegetation recovery typically begins. On the other hand, an undisturbed point, would be one covered by trees in all VHR images, and it should be guaranteed that there are no significant changes to the coverage of the trees, as some changes may be caused by

subtle forest disturbances between any two years. Ideally, as for small study area, randomly selected validation points covering the large study area should be used, but this is not possible with the limited available VHR images in Google Earth during 2015-2019. Fortunately, Google Earth VHR images exist during 2016-2019 covering different subset regions in the large study area. Therefore, 711 validation points outside the small study area (see Figure 1(a)) were extracted from the subset VHR images. Although the availability of VHR images varied in time and by region, thus, constraining the study, it helped greatly to extract sample points for each year. This approach provides a basis to evaluate the accuracy with which sample cases are defined as disturbances from 2016 to 2019.

3. Methodology

A central goal of this work is to produce a forest disturbance map at a fine spatial resolution of 10 m. This goal is achieved using the following three-stage process (see Figure 2):

(1) Landsat and Sentinel-2 annul maximal *r*NBR image generation. NBR images are calculated from each available Landsat-7/8 and Sentinel-2 scene from Jan. 2016 to Oct. 2019, and a self-referencing step is used to normalize each of the NBR images. By selecting the maximum self-referenced NBR (*r*NBR) value per-pixel for each observation period, the yearly composited Landsat (30 m) and Sentinel-2 (10 m) *r*NBR images are generated. This step can be performed in the GEE platform with the Forest Canopy Disturbance Monitoring (FCDM) tool proposed by Langner et al. (2018).

(2) Fusion of Landsat and Sentinel-2 *r*NBR images. A deep learning based downscaling method is used to predict the fine-resolution (10 m) annual *r*NBR images from the 30 m annual Landsat *r*NBR images by using the 10 m Sentinel-2 *r*NBR images during 2016-2019 as the training dataset. Then, for each year from 2016 to 2019, the downscaled 10 m Landsat *r*NBR and original Sentinel-2 *r*NBR images are fused to produce the 10 m integrated *r*NBR images by choosing the maximal value between them.

(3) Forest disturbance map production. The forest cover map generated from the Landsat TCC product in 2015 is used to mask the non-forest areas in all of the above-generated 10 m annual integrated *r*NBR images during 2016-2019, which are then used to produce the final fine-resolution forest disturbance map, where the disturbed year of each pixel is chosen as the year holding the maximal *r*NBR value in the time-series *r*NBR images.

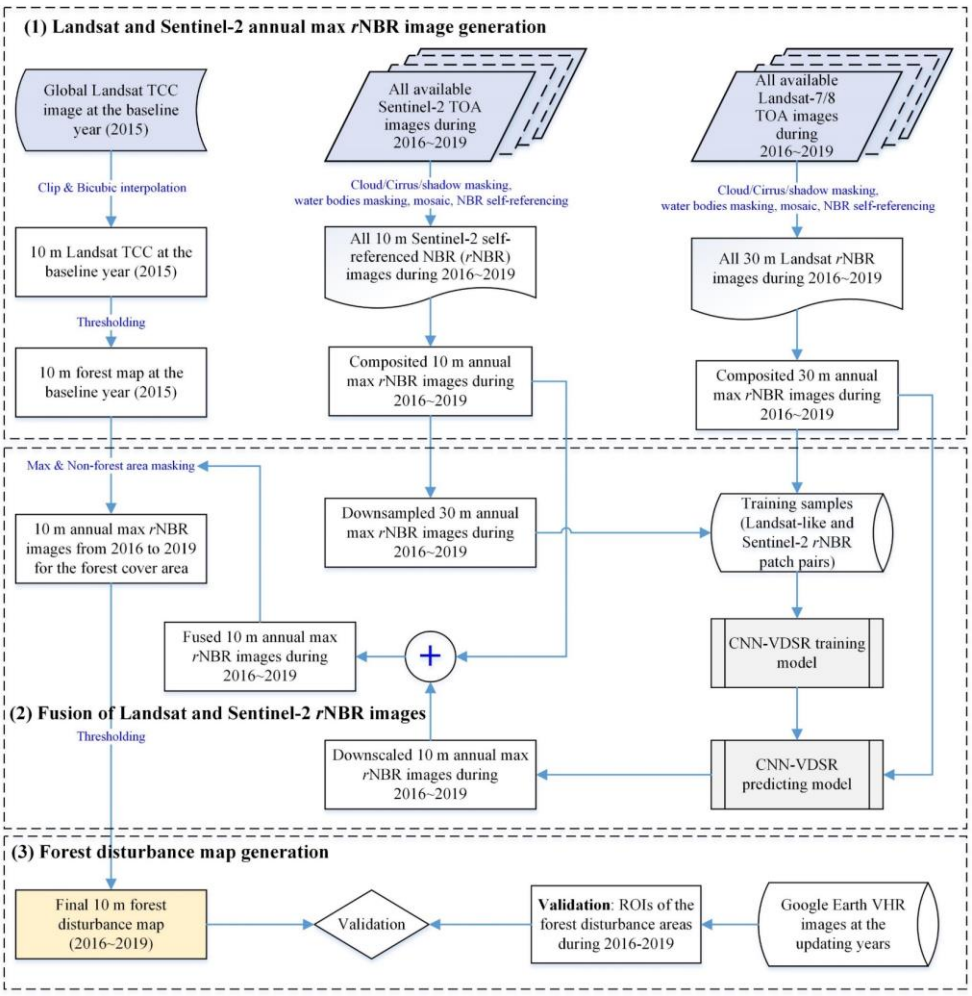

Figure 2. The proposed methodology.

3.1 NBR calculation and self-referencing

For all of the cloud and cloud-shadow masked single Landsat-7/8 and Sentinel-2 TOA images, the NBR vegetation index based on the near infrared (NIR) and the short-wavelength infrared (SWIR2) bands is calculated from equation 1,

$$\mathrm{NBR} = \frac{\rho(NIR) - \rho(SWIR_2)}{\rho(NIR + \rho(SWIR_2)} \quad (1)$$

where $\rho(NIR)$ is the TOA reflectance value of Landsat-7 ETM+ band 4 (0.78-0.90μm), Landsat-8 OLI band 5 (0.85-0.88μm), and Sentinel-2 MSI band 8 (0.78-0.90μm), and $\rho(SWIR_2)$ is the TOA reflectance value of Landsat-7 ETM+ band 7 (2.09-2.35μm), Landsat Landsat-8 OLI band 7 (2.11–2.29μm), and Sentinel-2 MSI band 12 (2.10-2.28μm). As the spatial resolution of the Sentinel-2 MSI band 12 is 20 m, a bicubic interpolation is carried out to transform it to a 10 m spatial resolution. The magnitude of NBR lies on a scale ranging from -1 to 1. Within the evergreen rainforests, a larger NBR value indicates generally a closed tree canopy crown cover, while a smaller NBR value indicates

openings in the closed tree canopy, in which exposed bare soil or non-photosynthetic vegetation components may contribute to the measured spectral response (Kennedy et al. 2010; Langner et al. 2018). It is noteworthy that openings are caused mostly by the logging of a small number of trees, often a single commercially valuable tree, and the NBR index is, therefore, able to monitor forest loss.

To reduce the gradual changes caused by the different atmospheric conditions or illumination/terrain-related geometries for each scene of the NBR signal, but retain any locally abrupt small-scale alteration of NBR values caused by human disturbances such as selective logging activities, a self-referencing step is introduced for each of the above cloud and cloud-shadow masked NBR scenes. The self-referencing step is expressed in equation 2.

$$r\mathrm{NBR} = \mathrm{NBR}(median, r) - \mathrm{NBR} \quad (2)$$

where NBR(*median*, *r*) is the median image calculated from the above-derived NBR image using a moving window. Specially, the pixel values in the NBR(*median*, *r*) image are the median value of the neighboring pixels contained in a circular moving kernel window centred on each pixel in the original NBR image. The radius (*r*) of the circular moving kernel window is 210, which corresponds to 7 pixels for Landsat images and 21 pixels for Sentinel-2 images. *r*NBR is the self-referenced NBR values, it will be close to 0 for undisturbed canopy cover, and presents positive values close to 1 for openings in the canopy cover. As the aim is to detect bare soil or non-photosynthetic vegetation caused by openings in the canopy cover, *r*NBR values between 0 and 1 are, therefore, expected. Any negative values of *r*NBR are neglected by setting them to 0 (negative value indicates very dense canopy crown cover), while values above 1 (these extreme values usually refer to active fires) are capped by setting them to 1. As shown in equation (3), by selecting the per-pixel maximum value of each *r*NBR image for each observation period of all above-masked Lansat-7/8 and Sentinel-2 NBR scenes, we create yearly composites of these *r*NBR values (namely as $r\mathrm{NBR}_{\mathrm{max}\_y}$), to reflect the most open canopy cover condition for the given year and capture any opening in the canopy caused by the human activities of selective logging and smallholder clearing.

$$r\mathrm{NBR}_{\mathrm{max}\_y} = \max_{01.01.y \le i \le 31.12.y} (r\mathrm{NBR}_i), \quad \text{where } y \in \{2016, \cdots, 2019\} \quad (3)$$

Where *y* refers to the year. By using the above method, the yearly composited maximal Landsat *r*NBR and Sentinel-2 *r*NBR images from 2016 to 2019 are then generated.

3.2 Deep-learning based downscaling of Landsat *r*NBR index images

The yearly composited Landsat *r*NBR images generated have a spatial resolution of 30 m and the aim is to downscale these data to the 10 m spatial resolution of the Sentinel-2 imagery. This downscaling is achieved using a deep learning approach to image super-resolution analysis (Dong et al. 2016; Kim et al. 2016a; Ling et al. 2019; Ling and Foody 2019). A convolutional neural network (CNN) model is used for the spatial downscaling of Landsat *r*NBR index images to ensure that the downscaled Landsat *r*NBR index images have the same fine spatial resolution as the Sentinel-2 *r*NBR images. The CNN model used in the downscaling analysis aims to model the potentially nonlinear relationship between the coarse resolution Landsat *r*NBR index images and the corresponding fine resolution Sentinel-2 *r*NBR index images. Instead of using directly the Landsat *r*NBR images as the coarse-resolution training dataset, the Landsat-like *r*NBR index images generated from the Sentinel-2 *r*NBR index images spatially degraded with scale factor 3 are used as the coarse-resolution *r*NBR images.

The whole procedure for downscaling the Landsat *r*NBR images comprises three steps: training sample generation, CNN model training, and finally, applying the trained CNN model to the real Landsat *r*NBR index images for downscaling. Training samples are extracted from the yearly composited Sentinel-2 *r*NBR index images and corresponding down-sampled Landsat-like *r*NBR index images during 2016-2019. Each of the training samples consists of a data pair: (i) a coarse-resolution Landsat-like *r*NBR index patch containing $M_1 \times M_2$ pixels and (ii) its corresponding fine-resolution Sentinel-2 *r*NBR index patch containing $(M_1 \times s) \times (M_2 \times s)$ pixels, where the values of M_1 and M_2 are set to 30, and s is the zoom factor which is set to 3 in this study. We finally select 3000 coarse-resolution and fine-resolution *r*NBR index patch pairs as the training samples. With the training samples, a very deep CNN approach, namely as VDSR (Kim et al. 2016a), is used to train the CNN model. VDSR contains 20 layers, where the first input layer is a 2-D convolutional layer, the 2~19 layers are 18 alternating convolutional and rectified linear unit layers, and the last layer consists of a single filter with a spatial size of 3×3×64. The input data to the VDSR training model is the coarse-resolution Landsat-like *r*NBR index patches in the training samples after application of a bicubic interpolation, so as to ensure they have the same spatial size (90×90 pixels) as those fine-resolution Sentinel-2 *r*NBR index patches. The difference between the interpolated Landsat-like *r*NBR index image and the corresponding fine-resolution Sentinel-2 *r*NBR index image in the training samples is used as the output of the VDSR training model. Therefore, the VDSR training model aims to learn the nonlinear relationship between the interpolated and the residual *r*NBR index images calculated from the training samples. Once the VDSR training model has been fitted,

it can be applied to real Landsat *r*NBR index images for downscaling. Each of the above-derived coarse-resolution Landsat *r*NBR index images from 2016 to 2019 are first interpolated with spatial scale 3 to form the fine-resolution (10 m) image, and a residual *r*NBR index image is then predicted from the interpolated image using the VDSR prediction model, and a fine-resolution *r*NBR index image is produced by adding the interpolated and the generated residual *r*NBR index image. We could, thus, obtain the downscaled annual fine-resolution (10 m) Landsat *r*NBR index images for 2016 to 2019.

3.3 Forest disturbance mapping by fusing 10 m Landsat and Sentinel-2 *r*NBR images

Firstly, the Sentinel-2 *r*NBR index images and the downscaled fine-resolution 10 m Landsat *r*NBR index images for the period from 2016 to 2019 are fused, in which the value of a pixel in the fused *r*NBR images is the maximal value observed for it in the downscaled Landsat *r*NBR and Sentinel-2 *r*NBR images. Secondly, the annual fused fine-resolution *r*NBR images during 2016-2019 are used to produce the maximal *r*NBR image, namely $r\mathrm{NBR}_{\max}$, where each pixel therein is determined as the maximal value of the four *r*NBR values from 2016 to 2019 (equation (4)).

$$r\mathrm{NBR}_{\max} = \max_{2016 \le y \le 2019} (r\mathrm{NBR}_{\max\_y}) \tag{4}$$

Thirdly, the Landsat TCC image in 2015 is downscaled to the spatial resolution of 10 m using a bicubic interpolation, and a threshold value of 30% is used to produce the baseline forest cover map in 2015 (Kim et al. 2014). For the forest covered area in the baseline forest cover map, if the corresponding pixel value in the $r\mathrm{NBR}_{\max}$ image is larger than a threshold value of δ, it will be regarded as a forest disturbed pixel and the disturbed year is the year that achieved the maximal *r*NBR value. This process is represented as

$$\text{forest disturbance map} = \begin{cases} y \in \{2016, \cdots, 2019\}, & \text{if } r\mathrm{NBR}_{\max} > \delta \\ 0 \end{cases}. \tag{5}$$

Finally, from this procedure, the forest disturbance map (disturbed year map) from 2016-2019 with a spatial resolution of 10 is produced.

3.4 Datasets and evaluation

With respect to the validation of the proposed method for mapping small-scale tropical forest disturbance, evaluations with both a spatially degraded Sentinel-2 data set and real Sentinel-2 and Landsat data set are designed. In the spatially degraded Sentinel-2 data evaluation, annual maximal Sentinel-2 *r*NBR images covering the small study area are degraded spatially with a factor of 3 to

generate annual maximal Landsat-like *r*NBR images. The setup of this evaluation aims to provide a full reference image to validate the accuracy of the resultant fine-resolution downscaled 10 m Landsat *r*NBR images and the generated 10 m forest disturbance map, so as to provide a comprehensive quantitative assessment of the performance of the deep-learning based downscaling method. In the evaluation based on real Sentinel-2 and Landsat data, the annual maximal Landsat and Sentinel-2 *r*NBR images during 2016-2019 are used as input, not only to validate the performance of the deep-learning based downscaling method, but more importantly to validate the strategy of fusing downscaled Landsat *r*NBR images and Sentinel-2 *r*NBR images in improving the monitoring ability of small-scale tropical forest disturbance.

3.5 Accuracy assessment

In the evaluation based on spatially degraded Sentinel-2 data, the Sentinel-2 *r*NBR images covering the small study area are used as reference, and five quantitative indices (correlation coefficient (CC), universal image quality index (UIQI), relative global dimensional synthesis error (ERGAS), root mean square error (RMSE), and average absolute deviation (AAD) (Garzelli and Nencini 2009)) are used to provide a quantitative assessment of the downscaled Landsat-like *r*NBR images generated by the deep-learning based downscaling method. Moreover, using the forest disturbance map generated from the annual Sentinel-2 *r*NBR images as reference, the indices of overall classification accuracy (OA) and the class-level accuracy expressed as producer's and user's accuracy are used to validate the forest disturbance map generated from the deep-learning based downscaling method.

For validation of the resultant forest disturbance map based on the real Sentinel-2 and Landsat data in the small study area, we focus on 988 randomly selected points, including 429 undisturbed points, 151 disturbance points in 2016, 107 disturbance points in 2017, 150 disturbance points in 2018, and 151 disturbance points in 2019 (see Figure 1(c)). For the large study area, it would be preferable to use randomly selected validation points as the small study area, but this is not possible with the data available in Google Earth for 2015-2019 (Du et al. 2016). As mentioned above, some Google Earth VHR images during 2016-2019 covering different subset regions in the large study area were used finally to extract the limited number of validation points. In total, as shown in Figure 1(a), 711 validation points were extracted outside the small study area, including 79 undisturbed points, 369 disturbance points in 2016, 65 disturbance points in 2017, 39 disturbance points in 2018, and 159 disturbance points in 2019.

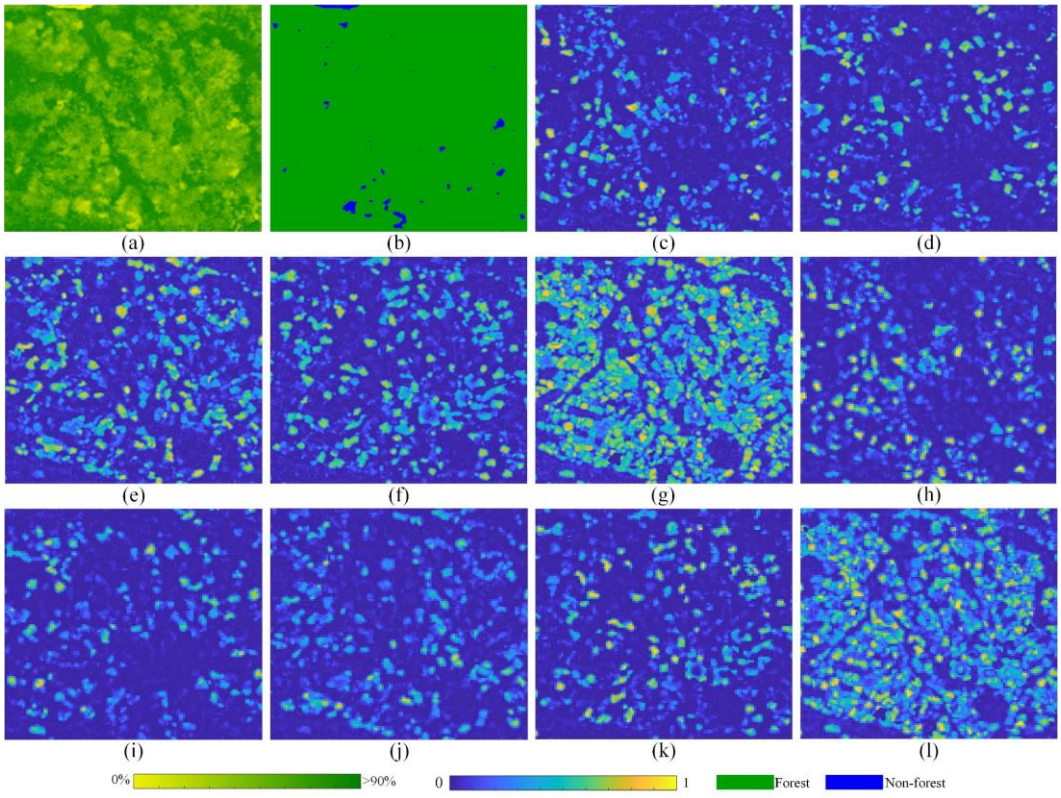

Figure 3. Input data for the spatially degraded Sentinel-2 data evaluation. (a) subset Landsat TCC image at 2015 (120 pixels × 120 pixels); (b) subset forest cover map at 2015; (c)-(f) subset Sentinel-2 *r*NBR images from 2016 to 2019, respectively (360 pixels × 360 pixels); (g) subset maximal Sentinel-2 *r*NBR image during 2016-2019; (h)-(k) subset Landsat-like *r*NBR images from 2016 to 2019, respectively; (l) subset maximal Landsat-like *r*NBR image during 2016-2019.

4. Results

4.1 Spatially degraded Sentinel-2 data evaluation

The input data for this spatially degraded Sentinel-2 data evaluation is based on the small study area (see Figure 3). For the Sentinel-2 and Landsat *r*NBR images, the larger the value of *r*NBR, the higher the possibility of a disturbance event, and these *r*NBR images are taken to be the probability of forest disturbance. Based on the forest cover area in 2015 in Figure 3(b), we can see from Figure 3(g) that most pixels are covered by small areas with high *r*NBR value, which indicates that forest disturbance events occurred frequently during 2016-2019. For the Landsat-like *r*NBR images, there are typically jagged boundaries around many areas with high *r*NBR value unlike the original fine-resolution Sentinel-2 *r*NBR images. Therefore, with its finer spatial resolution, Sentinel-2 can represent more spatial detail about small-scale forest disturbance than the Landsat image. To overcome the lack of fine spatial resolution for Landsat *r*NBR image in tracking small-scale forest disturbance events, spatial downscaling methods,

including traditional bicubic interpolation and the above-mentioned CNN-VDSR, were used in this research to increase the spatial resolution of the Landsat *r*NBR images, and the results are shown in Figure 4.

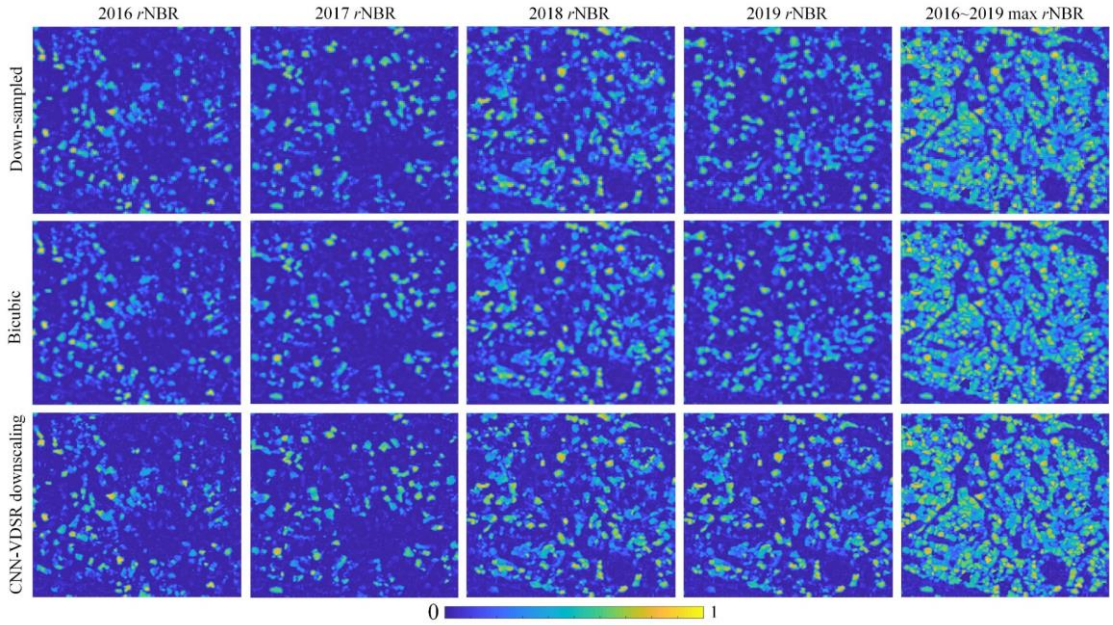

Figure 4. (TOP) Down-sampled 30 m Landsat-like annual maximal *r*NBR images, (middle) bicubic interpolated 10 m Landsat-like annual max *r*NBR images and (bottom) CNN-VDSR downscaled 10 m Landsat-like annual max *r*NBR images from 2016 to 2019 in the spatially degraded Sentinel-2 data evaluation.

From comparison of the CC, UIQI, ERGAS, RMSE, and AAD values listed in Table 2 and the *r*NBR images shown in Figure 4, it is evident that important boundary information associated with small areas of disturbance in the down-sampled Landsat-like *r*NBR images are lost, and the corresponding quantitative indices of CC and UIQI stay low, while the ERGAS, RMSE, and AAD are high. After the use of bicubic interpolation, the jagged boundaries around many small-scale areas become spatially smooth, and the CC and UIQI values increase to more than 0.97, where there is also an obvious decrease of the ERGAS, RMSE, and AAD values. However, it is noted that the boundaries of many small-scale areas in the bicubic interpolated results are over-smoothed and spatially blurred. For the results of CNN-VDSR downscaling, the jagged boundaries also become spatially smooth, and the issue of boundary blurring around the small-scale areas is greatly improved. Comparing with the results of bicubic interpolation, all of the *r*NBR images generated by CNN-VDSR downscaling illustrate greater spatial detail of the forest disturbance process, and are more similar to the reference Sentinel-2 *r*NBR images. Moreover, the CNN-VDSR downscaling results have the highest CC and UIQI values, and smallest

ERGAS, RMSE, and AAD values, which demonstrates the advantage of the CNN-VDSR method in downscaling Landsat-like *r*NBR images.

Table 2. Quantitative assessment of the Landsat-like *r*NBR images and the spatially downscaled *r*NBR images by using the Sentinel-2 *r*NBR images as a reference in the spatially degraded Sentinel-2 data evaluation.

	Year	CC	UIQI	ERGAS	RMSE	AAD
Down-sampled (Landsat-like)	2016	0.9398	0.9380	21.1487	0.0508	0.0263
	2017	0.9460	0.9445	20.7541	0.0494	0.0249
	2018	0.9446	0.9431	15.5220	0.0635	0.0364
	2019	0.9467	0.9453	16.4062	0.0580	0.0324
	Max (2017-2019)	0.9361	0.9339	10.1753	0.0859	0.0567
Bicubic interpolation	2016	0.9762	0.9727	13.8917	0.0334	0.0199
	2017	0.9801	0.9773	13.1445	0.0313	0.0186
	2018	0.9790	0.9761	9.9699	0.0408	0.0264
	2019	0.9810	0.9783	10.2379	0.0362	0.0233
	Max (2017-2019)	0.9786	0.9737	6.3592	0.0537	0.0383
CNN-VDSR downscaling	2016	0.9852	0.9848	10.6538	0.0256	0.0159
	2017	0.9885	0.9882	9.7054	0.0231	0.0146
	2018	0.9875	0.9872	7.4828	0.0306	0.0204
	2019	0.9895	0.9892	7.3858	0.0261	0.0174
	Max (2017-2019)	0.9883	0.9878	4.4383	0.0375	0.0264

To provide a clear visual comparison of the resultant *r*NBR images in Figure 4, error maps between the *r*NBR images of down-sampling, bicubic interpolation, CNN-VDSR downscaling and the original reference Sentinel-2 *r*NBR images were generated. As shown in the first row of Figure 5, it is obvious that lots of jagged red and blue pixels appear around the boundaries of the small disturbed areas in the down-sampled *r*NBR error maps. This is because, compared to the reference Sentinel-2 *r*NBR image, many *r*NBR values were overestimated (e.g. red pixels) in the down-sampled Landsat-like *r*NBR images, while some *r*NBR values were underestimated (e.g. blue pixels). For the error maps generated from the bicubic interpolated *r*NBR images, fewer red and blue pixels are found, but the outlines of many disturbed areas are still clearly visible. For example, some red pixels are around the outside of the small disturbed areas, while some blue pixels are within the disturbed areas. However, for the CNN-VDSR downscaled *r*NBR error maps, the number of red and blue pixels decreases significantly, and we can hardly see the outline of the disturbed areas appearing in the error maps for down-sampling and bicubic interpolation.

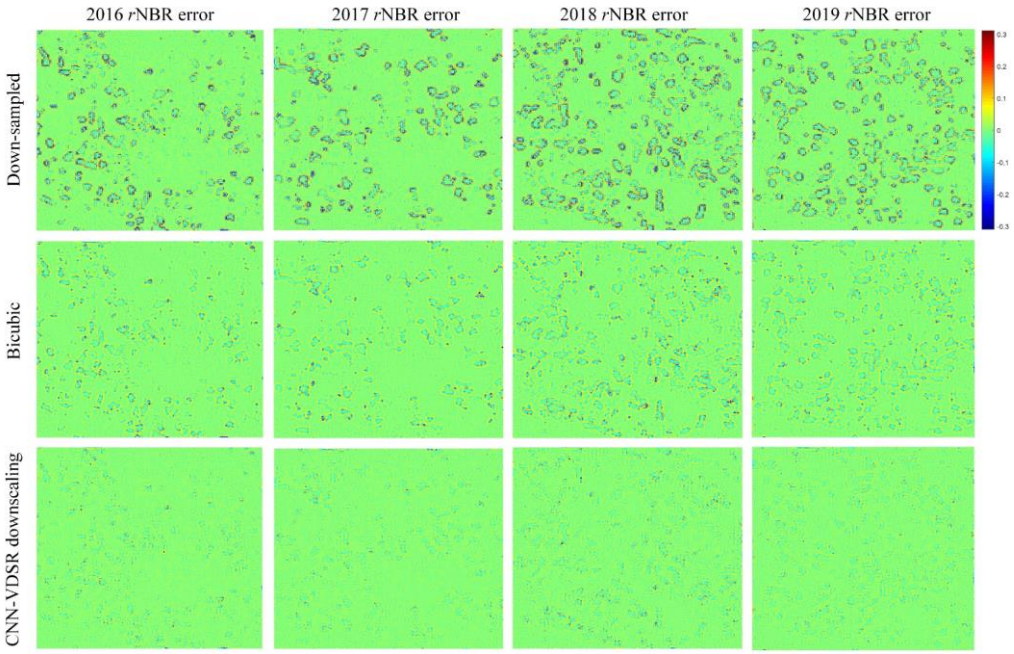

Figure 5. Error maps of the (top) down-sampled Landsat annual maximal *r*NBR images, (middle) bicubic interpolated annual maximal *r*NBR images and (bottom) CNN-VDSR downscaled annual maximal *r*NBR images during 2016-2019 in Figure 4.

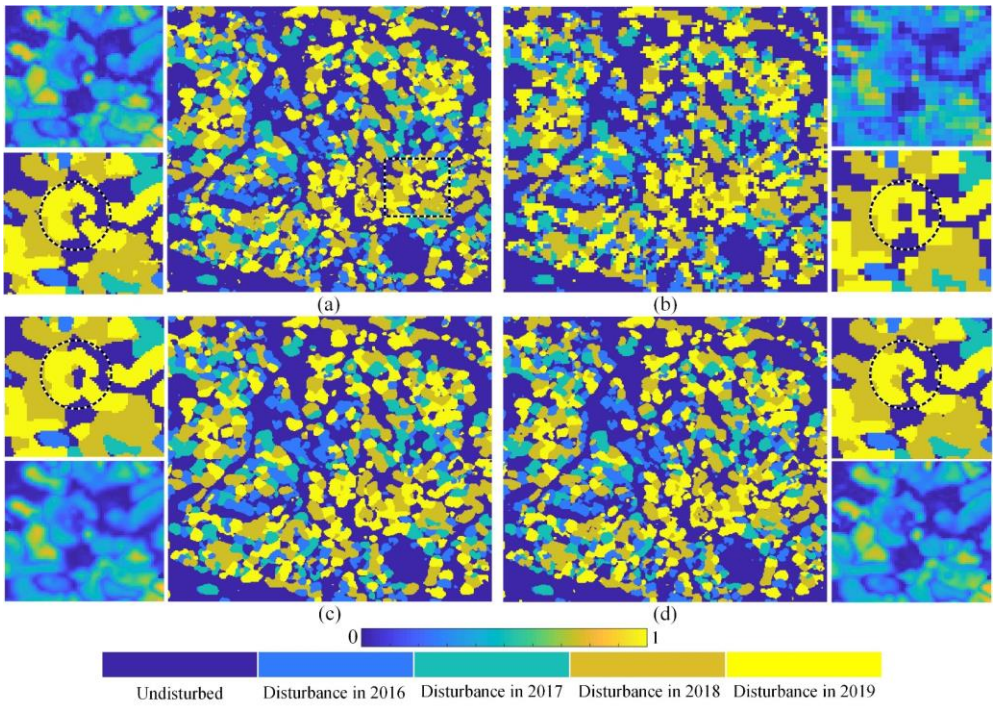

Figure 6. Reference and resultant forest disturbance maps and corresponding maximal *r*NBR images in the spatially degraded Sentinel-2 data experiment. (a) Reference Sentinel-2 forest disturbance map; (b) Landsat-like forest disturbance map; (c) Bicubic interpolation based forest disturbance map; (d) CNN-VDSR downscaling based forest disturbance map.

As the non-forest area in 2015 (see Figure 3(b)) was masked and set to be zero in the *r*NBR images, the above generated maximal *r*NBR images in Figure 4 can, thus, be regarded as forest disturbance

possibility maps during 2016-2019, and a threshold value is needed to produce the final forest disturbance map. The threshold value was set to be 0.14, as it can track the most accurate forest disturbance areas in the real experiment: more discussion will be presented on this choice in the following section. Figure 6 shows the reference and resultant forest disturbance maps produced using the threshold value of 0.14, where any pixel value in the maximal *r*NBR images larger than 0.14 is regarded as a disturbed pixel, and the corresponding year that generates the maximal *r*NBR pixel value is viewed as the disturbed year. Table 3 lists the OA, producer's accuracy and user's accuracy of the resultant forest disturbance maps by using Sentinel-2 forest disturbance map as reference.

Table 3. Accuracy assessment (Overall accuracy, Producer's and User's accuracy) of the forest disturbance maps generated by different methods in the spatially degraded Sentinel-2 data experiment.

	OA	Producer's accuracy for disturbance					User's accuracy for disturbance				
		Undisturbed	2016	2017	2018	2019	Undisturbed	2016	2017	2018	2019
Down-sampled (Landsat-like)	87.95%	88.84%	83.40%	87.29%	88.96%	88.19%	92.02%	82.90%	85.65%	86.20%	85.44%
Bicubic interpolation	93.07%	90.96%	90.32%	95.18%	96.24%	95.26%	97.35%	90.12%	91.15%	90.11%	90.26%
CNN-VDSR downscaling	95.22%	95.35%	92.38%	95.38%	96.31%	95.56%	96.79%	93.16%	94.64%	94.34%	94.23%

As shown in Figure 6, by comparing with the reference forest disturbance map, the Landsat-like forest disturbance map has jagged boundaries. This is due to the spatial resolution of Landsat images being too coarse to represent the spatial detail of many small-scale forest disturbances. A similar trend in *r*NBR images (see Figure 4) can also be observed for the bicubic interpolation-based forest disturbance map, the jagged boundaries become spatially smooth, and the OA increases by 5.12% compared with that of the Landsat-like forest disturbance map. Compared with the reference forest disturbance map shown in Figure 6(a), almost all the forest disturbance areas in the map produced by bicubic interpolation look too large; although this results in low commission error, it will also lead to a high level of omission error around the boundaries. However, for the result of CNN-VDSR downscaling, the issues of jagged and inflated boundaries are overcome, and more details about the spatial patterns of various disturbance areas are well maintained and more similar to the reference forest disturbance map, which can also be confirmed by significantly increasing OA, producer's and user's accuracy in Table 3.

For this synthetic data experiment, the disturbed areas of the reference and resultant forest disturbance maps during 2016-2019 for different methods are listed in Table 4, and the area error percentages between the reference and resultant forest disturbance areas are also listed. It is noted that the areas in both 2016 and 2017 are about ~1.4 km^2, in both 2018 and 2019 are about ~2.3 km^2, and the

total area during 2016-2019 is 7.5755 km^2. For the down-sampled Landsat-like result, the total forest disturbance area is overestimated by 2.45%. As mentioned above, the result of bicubic interpolation is more accurate than the down-sampled Landsat-like result, but the total forest disturbance area is overestimated by 4.67%, which is almost twice that of the down-sampled Landsat-like result. This is due to the serious issue of inflated boundaries in the bicubic interpolation result. However, for the CNN-VDSR downscaling, the estimated disturbed area is closest to the reference, overestimated by only 1.05%; less than a quarter of the error for bicubic interpolation.

Table 4. Disturbed areas (and area errors) of the reference Sentinel-2 forest disturbance map and the resultant forest disturbance maps generated by different methods in the spatially degraded Sentinel-2 data experiment.

	Km^2	Disturbance year				
		2016	2017	2018	2019	Total (2016~2019)
Reference Sentinel-2	area	1.4841	1.4424	2.3298	2.3192	7.5755
Down-sampled (Landsat-like)	area	1.4931	1.47	2.4043	2.394	7.7614
	area error	0.61%	1.91%	3.20%	3.23%	2.45%
Bicubic interpolation	area	1.4873	1.5062	2.4881	2.4477	7.9293
	area error	0.22%	4.42%	6.79%	5.54%	4.67%
CNN-VDSR downscaling	area	1.4716	1.4536	2.3783	2.3519	7.6554
	area error	-0.84%	0.78%	2.08%	1.41%	1.05%

4.2 Real Sentinel-2 and Landsat data evaluation

Unlike the above spatially degraded Sentinel-2 data evaluation, real Landsat-7/8 and Sentinel-2 *r*NBR images during 2016-2019 were used directly as the input data in the real Sentinel-2 and Landsat data evaluation. For the small study area dataset (see Figure 1(b)), Figure 7 shows the subset (covering the same study area in the above data evaluation) maximal *r*NBR images and resultant forest disturbance maps of different methods. The corresponding accuracy assessment of these subset forest disturbance maps is listed in Table 5 by using the randomly selected 988 validation points as the reference. To go from the maximal *r*NBR image to the final forest disturbance map, an empirically-derived threshold value is needed, and the effect of the threshold value on the forest disturbance map is evaluated in the following sections. With the mean *r*NBR image generated from the annual fused *r*NBR images during 2016-2019, the detection of forest disturbance events which occurred more than once is analyzed and discussed. For the large study area dataset (see Figure 1(a)), with the proposed method based on the fusion of Sentinel-2 and CNN-VDSR downscaled Landsat-7/8 *r*NBR images during 2016-2019, the maximal fine-resolution (10 m) *r*NBR image and resultant forest disturbance map covering the whole

study area are illustrated in Figure 10. Table 6 lists the disturbed areas of the resultant forest disturbance maps during 2016-2019 for different methods, and the accuracy assessment of the generated forest disturbance maps is listed in Table 7.

4.2.1 Small study area dataset

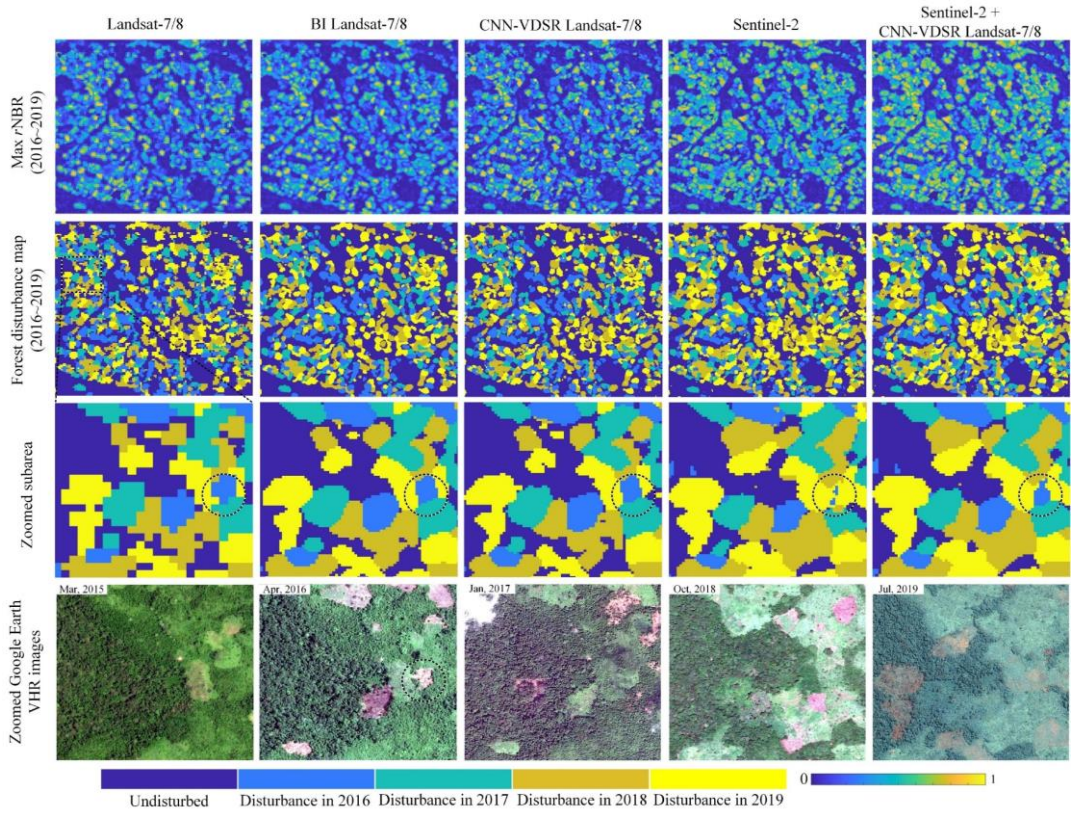

Figure 7. The maximal *r*NBR image, resultant forest disturbance map and Google Earth VHR image for the real Sentinel-2 and Landsat data evaluation based on the small study area. (First row) maximal *r*NBR images during 2016-2019, (second row) forest disturbance maps during 2016-2019, (third row) zoomed subarea of the forest disturbance maps, and (fourth row) zoomed subarea of the Google Earth VHR images.

Table 5. Accuracy assessment (Overall accuracy, Producer's and User's accuracy) of the forest disturbance maps generated by different methods in the real Sentinel-2 and Landsat data evaluation for the small study area.

	OA	Producer's accuracy for disturbance					User's accuracy for disturbance				
		Undisturbed	2016	2017	2018	2019	Undisturbed	2016	2017	2018	2019
Landsat-7/8	78.95%	85.40%	81.65%	75.00%	74.16%	69.54%	80.14%	62.68%	76.99%	89.80%	81.76%
Bicubic interpolation	81.88%	86.86%	88.07%	76.72%	79.21%	72.41%	83.22%	63.58%	83.18%	94.00%	83.44%
CNN-VDSR downscaling	83.00%	90.22%	88.07%	77.59%	77.53%	72.16%	82.00%	67.61%	84.91%	95.83%	86.99%
Sentinel-2	86.03%	87.53%	84.40%	79.31%	91.57%	82.39%	90.86%	73.02%	89.32%	87.63%	81.01%
Proposed (Sentinel-2 + CNN-VDSR)	87.45%	83.70%	95.41%	84.48%	92.13%	88.51%	95.03%	70.27%	89.09%	90.11%	82.80%

For the small study area, as shown in the first row of Figure 7, most of the *r*NBR values of the Sentinel-2 image are larger than those of the Landsat-7/8 based *r*NBR image, which indicates that

Sentinel-2 images could capture more forest disturbance events than the Landsat-7/8 images. For the resultant forest disturbance maps, a similar trend as that shown in the synthetic experiment can also be observed. The boundaries in the Landsat-7/8 results are represented as jagged patterns, and it is difficult to determine the detailed spatial distribution of the small-scale forest disturbances, leading to the smallest OA value of 78.95% (see Table 5). For bicubic interpolation and CNN-VDSR downscaling, the jagged boundaries become spatially smooth, but the boundaries of bicubic interpolation result are over-smoothed, while the spatial patterns of various disturbed areas in the CNN-VDSR downscaling result represent more details learned from the Sentinel-2 images. This is why the CNN-VDSR downscaling result achieved greater accuracy than the bicubic interpolation result. Sentinel-2 produced spatially smooth boundaries that are more similar to the time-series zoomed Google Earth VHR images, and more disturbed areas were captured that Landsat-7/8 could not detect. This is because Sentinel-2 images have a finer spatial resolution to represent more spatial detail about various forest disturbance patterns, and have a finer temporal resolution to detect more disturbed area in the short term. Conversely, there are some disturbed areas that Landsat-7/8 images can detect, but Sentinel-2 images cannot find. For example, the disturbed area in the circles of Figure 7 occurred in Apr. 2016, and it was detected by the results generated from Landsat-7/8 images, but the Sentinel-2 result did not identify it. However, as shown in the result produced by fusing the Sentinel-2 and CNN-VDSR downscaled Landsat-7/8 *r*NBR images, it not only contains the disturbed areas detected by the Sentinel-2 images, but also those of the downscaled Landsat-7/8 images. Moreover, the result achieved the highest accuracy as shown in Table 5, where the OA value increased by 10.77% compared with the Landsat-7/8 result, and the OA value increased by 1.84% compared with the Sentinel-2 result, which indicates the superiority of the proposed method.

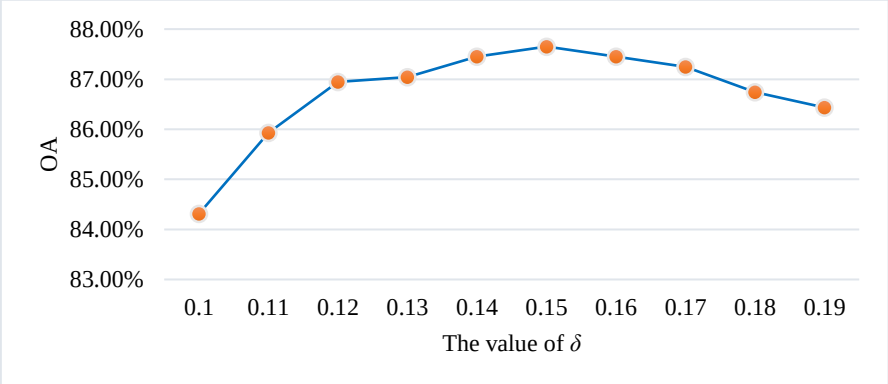

Figure 8. Overall accuracy (OA) values of the forest disturbance maps generated by the proposed method in which the value of δ is in the range of 0.1-0.19 with an interval of 0.01 for the small study area.

As presented in section 3.3, the threshold value δ has a key impact on the production of the final forest disturbance map. With the value of δ in the range of 0.10-0.19, the OA generated by the proposed method is shown in Figure 8. When δ is 0.10, although almost all of the forest disturbance events are detected, the OA is the smallest, because many undisturbed pixels are regarded as disturbed pixels. Thus, noise can be expected in the result when δ is too small. With an increase of δ from 0.10 to 0.15, the OA values increase. However, when δ is larger than 0.15, the OA value decreases monotonically, as many forest disturbance events, especially the small-scale forest disturbance of selective logging, cannot be detected when δ is too large. In general, when δ is assigned in a suitable range of 0.14-0.16, the resultant forest disturbance map achieved the optimal OA. In this research, δ was set to be 0.14 in the experiments, to map forest disturbances with maximum accuracy and detect subset forest disturbance events at the same time.

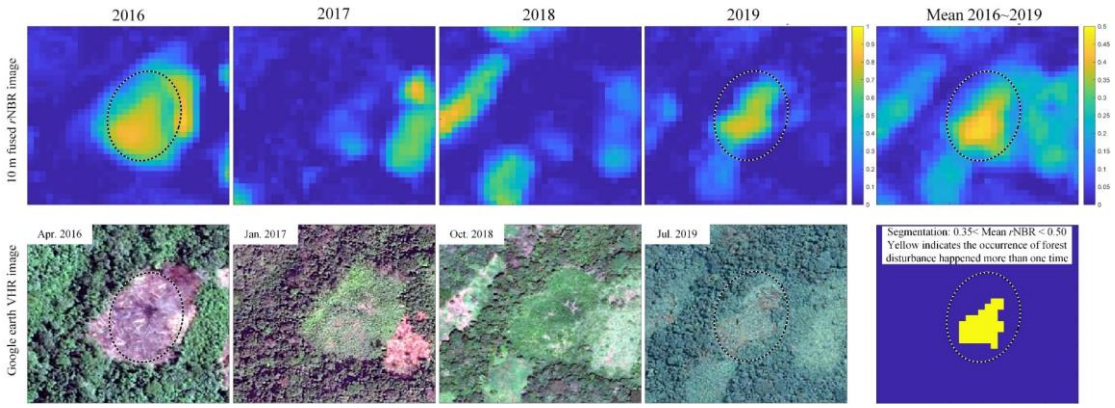

Figure 9. An example used to show small-scale forest disturbances that occur more than once. (Top) 10 m fused *r*NBR images during 2016-2019, (bottom) Google Earth VHR images during 2016-2019 and the resultant map showing forest disturbances that occurred more than once.

In this research, we use the annual fine spatial resolution *r*NBR images to generate a possibility map that identifies the occurrence of forest disturbance at more than one time. As shown in Figure 9, the mean subset *r*NBR image generated from the annual fine-resolution *r*NBR images during 2016-2019 can be used to track small-scale tropical forest disturbance events that occurred more than once. We empirically find that pixels with mean *r*NBR value larger than 0.35 and smaller than 0.50 are the most likely to be disturbed more than once. In Figure 9, the forest cover area in the ellipse was first disturbed in 2016, and the secondary forest recovered in the following two years. A disturbance event is detected again at this location in 2019. If the mean *r*NBR value is small (e.g., less than 0.35), it indicates that forest disturbance occurred only once; conversely, if the mean *r*NBR value is large (e.g., more than 0.50), it indicates that

the site is always covered by bare land, which may indicate settlement or an urban area. For the whole study area, by using this principle, we find that 1.42% of the total forest disturbance areas during 2016-2019 experienced multiple forest disturbances.

4.2.2 Full, large study area dataset

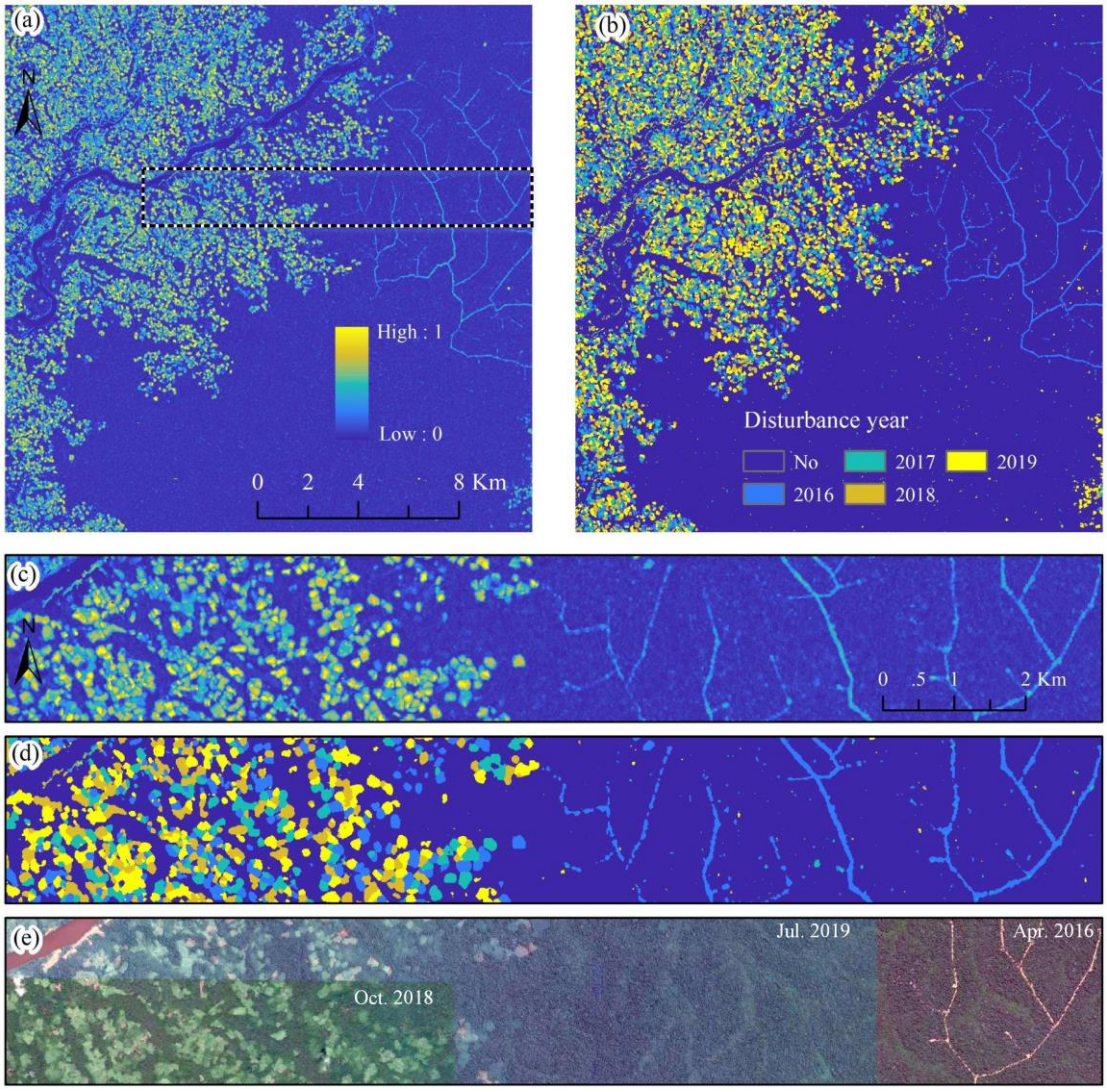

Figure 10. The max *r*NBR image, resultant forest disturbance map and Google Earth VHR image for the large study area in the real Sentinel-2 and Landsat data validation. (a) Maximal *r*NBR image during 2016-2019 by fusing Sentinel-2 and CNN-VDSR downscaled Landsat-7/8 *r*NBR images (2100 pixels × 2100 pixels); (b) Forest disturbance map generated from (a); (c) Zoomed subset maximal *r*NBR image of (a); (d) Forest disturbance map generated from (c); (e) The subset Google Earth VHR image.

By using the proposed method involving fusing the Sentinel-2 *r*NBR images and CNN-VDSR downscaled Landsat-7/8 *r*NBR images, the result covering the large study area is shown in Figure 10, and Table 6 lists the areas of the forest disturbance maps during 2016-2019 for the different methods.

With the resultant forest disturbance maps, it is easy to calculate the area of forest disturbance in each year during 2016-2019 by multiplying the total number of disturbed pixels for each year and the area of each pixel (e.g. 0.01km × 0.01km), but the error of resultant forest disturbance map cannot be considered by this way. To solve this problem, it is best to use the error matrix of the resultant forest disturbance map to decrease the uncertainty of area calculation (Olofsson et al. 2014); unfortunately, the error matrix was only available for the subset study area (Figure 1(c)) due to the lack of time-series VHR images covering the entire region (Figure 1(a)), and the error matrix calculated from the subset was not fully representative of the entire region. Therefore, as listed in Table 6, the area calculation based only on the pixel accounting was applied in the whole study area. From Table 6, we can see that for the disturbed areas only based on the Landsat-7/8 images, they are almost all less than that based on the Sentinel-2 images, and the total disturbed area of the Sentinel-2 result is increased by 9.16% compared with that of Landsat-7/8 result. However, for 2016, the disturbed area of the Landsat-7/8 result is larger than that of the Sentinel-2 result, which shows that there are still many disturbed areas that the Sentinel-2 based forest disturbance map cannot detect. The result based on the fusion of Sentinel-2 and CNN-VDSR downscaling based *r*NBR images achieved the largest disturbed areas for any year from 2016 to 2019, and the total area increased by 21.15% from that of the Landsat-7/8 result and increased by 11.43% compared to the Sentinel-2 result. This means that the proposed method could detect more (e.g., more than 11% to 21%) disturbed areas than any single data source of Sentinel-2 images or Landsat-7/8 images.

Table 6. The disturbed areas (km^2) of resultant forest disturbance maps during 2016-2019 for different methods in the real Sentinel-2 and Landsat data evaluation based on the larger study area.

	2016	2017	2018	2019	Total disturbance
Landsat-7/8	31.8165	20.8296	22.1486	22.9656	97.7603
Bicubic interpolation	32.7981	21.1662	22.7424	23.8561	100.5628
CNN-VDSR downscaling	31.7517	21.0570	22.4962	22.9081	98.2130
Sentinel-2	28.5985	21.3540	28.6643	28.0969	106.7137
Proposed (Sentinel-2 + CNN-VDSR)	35.1317	24.4371	28.9049	30.4415	118.9152

As shown in Figure 1(a), 711 validation points extracted outside the small study area were used as reference. The accuracy assessment of the forest disturbance maps generated by the different methods is listed in Table 7. The results for this large study area dataset validation are similar to those for the small study area (see Table 5). Due to the lack of detailed information on the spatial distribution of small-scale forest disturbances, the forest disturbance map generated directly from the Landsat-7/8 *r*NBR images has

the smallest OA, Producer's and User's accuracy values. Bicubic interpolation resulted in an increase in accuracy and CNN-VDSR downscaling increased the accuracy further. This indicates the superiority of CNN-VDSR downscaling over the bicubic interpolation for tracking small-scale tropical forest disturbances. Using Sentinel-2 data resulted in an increase in accuracy over the Landsat-7/8 for both Bicubic interpolation and CNN-VDSR downscaling. This is because Sentinel-2 images have finer spatial and temporal resolutions than Landsat images. However, fusing Sentinel-2 and CNN-VDSR downscaled Landsat-7/8 *r*NBR images produced the largest OA, Producer's and User's accuracy values. This means that the proposed method has strong extendibility and reliability for the accurate tracking of small-scale tropical forest disturbances in the large study area.

Table 7. Accuracy assessment (OA, Producer's and User's accuracy) of the forest disturbance maps generated by different methods in the real Sentinel-2 and Landsat data evaluation based on the large study area.

	OA	Producer's accuracy for disturbance					User's accuracy for disturbance				
		Undisturbed	2016	2017	2018	2019	Undisturbed	2016	2017	2018	2019
Landsat-7/8	90.58%	96.15%	93.30%	80.65%	74.42%	89.68%	70.75%	95.87%	90.91%	88.89%	92.05%
Bicubic interpolation	92.55%	93.59%	96.78%	82.26%	74.42%	90.97%	77.66%	96.27%	92.73%	94.12%	92.16%
CNN-VDSR downscaling	93.25%	98.72%	97.05%	82.26%	76.74%	90.32%	80.21%	96.79%	86.44%	94.29%	95.24%
Sentinel-2	95.78%	96.15%	95.17%	98.39%	88.37%	98.06%	90.36%	99.16%	88.41%	92.68%	95.00%
Proposed (Sentinel-2 + CNN-VDSR)	96.91%	97.44%	97.32%	96.77%	88.37%	98.06%	96.20%	98.37%	92.31%	97.44%	95.60%

5. Discussion

The above data evaluation and comparison with both spatially degraded Sentinel-2 data and real Sentinel-2 and Landsat data indicate mainly that: 1) the CNN-VDSR downscaled *r*NBR images were the most similar to the reference Sentinel-2 *r*NBR images and can produce forest disturbance map with better accuracy; 2) fusing the Sentinel-2 and CNN-VDSR downscaled Landsat-7/8 *r*NBR images can increase the accuracy of forest disturbance mapping and detect more disturbed areas that cannot be found with only Landsat or Sentinel-2 images. Some further issues are discussed in the following subsections.

5.1 Fusion of Sentinel-2 and Landsat data

The fusion of Sentinel-2 and Landsat data is currently a hot topic in the field of remote sensing image processing and application (Wang et al. 2017; Claverie et al. 2018; Shao et al. 2019), and most of them focus on the spatio-temporal fusion of surface reflectance. In this research, instead of fusing the Sentinel-2 and Landsat multispectral images first and then calculating the fused *r*NBR index images, we focus on the fusion of Sentinel-2 and Landsat *r*NBR images. This is because if the fusion is based on the

multispectral images, the three bands fused in the *r*NBR index need to be processed and many follow-up operations are required to track the final forest disturbance map; on the other hand, if the fusion is based on the *r*NBR images extracted from the Sentinel-2 and Landsat data, the results can be used directly to map forest disturbance. Thus, for tracking small-scale forest disturbance in this study, fusing the Sentinel-2 and Landsat *r*NBR images saves computation time. According to the research presented by Jarihani et al. (2014), for the production of multispectral indices, directly fusing the index images ("Index-then-Blend") produces more accurate results compared with the strategy of fusing multispectral images first and then calculating the fused index images ("Blend-then-Index"). Therefore, in this research, the Sentinel-2 and Landsat *r*NBR images were fused.

5.2 Areas disturbed multiple times

For most research involving the satellite-driven mapping of small-scale tropical forest disturbances, the disturbances are generally believed to happen only once. However, in the real situation, some parts of the forest may experience multiple disturbance events in time. For example, small-scale tropical forest disturbance associated with smallholder clearing will often be followed by a fast regrowth of vegetation, requiring further clearance to enable continued use of the land. As shown in Figure 9, the mean subset *r*NBR image generated from the annual fine-resolution *r*NBR images during 2016-2019 can be used to track the small-scale tropical forest disturbance events that occurred more than once. In general, multiple forest disturbances occur rarely and the disturbed areas are always small, especially in the short study period of 2016-2019. Therefore, the uncertainty of omission and commission errors in the tracking of small-scale forest disturbance (see Table 5 and Table 7) would affect inevitably the detection of areas that are disturbed multiple times. To decrease the uncertainty, we do not use directly the forest disturbance map of each year to detect the areas disturbed multiple times, but instead used the mean *r*NBR image extracted from the annual fused *r*NBR images during 2016-2019. This is because the omission or commission errors of forest disturbance for each year are around 10-30%, and such errors would transfer to the detection process of the area that experienced multiple forest disturbances if we use them directly. On the other hand, a relatively large threshold value was used to track areas disturbed multiple times from the mean *r*NBR image. This can guarantee that the tracked multiple forest disturbances have a relatively low commission error. Ideally, it is preferable to provide a quantitative evaluation of the areas disturbed multiple times, but in practice time-series VHR images used to provide the validation points

may not be available. In future research, more studies should be undertaken to decrease the uncertainty of tracking areas with multiple forest disturbances.

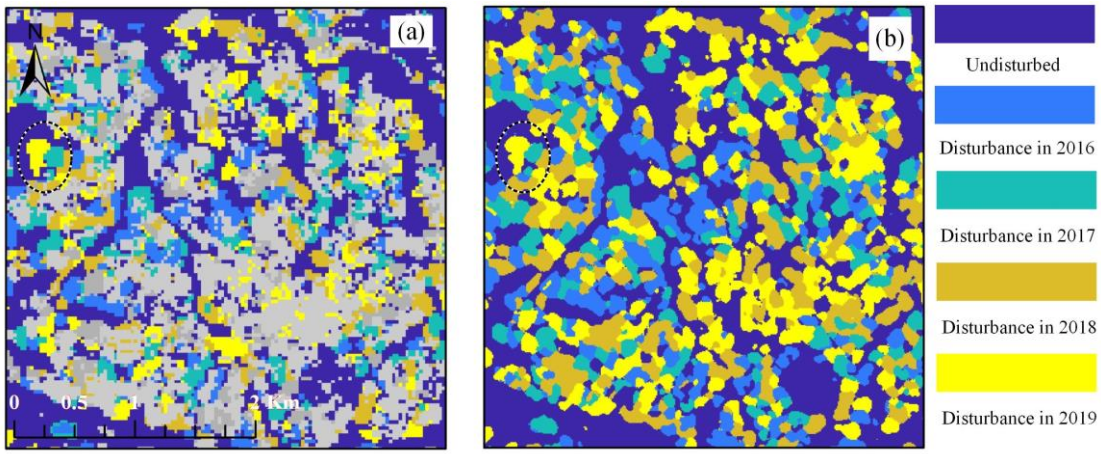

Figure 11. Comparison between Hansen's forest change map and the forest disturbance map produced by the proposed method. (a) Hansen's global forest change map at the small study area; (b) Forest disturbance map produced by the proposed method at the small study area.

5.3 Comparison and fusion with Hansen's global forest change map

It is noted that the global forest change map since 2000 produced by Hansen et al. (2013) can also be used to track forest disturbances happened in tropical forest areas. Figure 11 is used here to have a visual comparison between Hansen's global forest change map and forest disturbance map generated by the proposed method (fusing Sentinel-2 and CNN-VDSR downscaled Landsat-7/8 *r*NBR images) for the subset study area. As shown in Figure 11(a), forest disturbances happened during 2001-2015 were masked as a gray colour, so as to focus on the disturbed areas from 2016 to 2019. It is difficult to provide a quantitative accuracy comparison between the two products, as Hansen's product was based on the forest cover in 2000, while the proposed method was based on forest cover in 2015. However, in terms of visual comparison, the forest disturbance map of the proposed method shown in Figure 11(b) has a finer spatial resolution and more spatial detail about forest change was exploited, such as areas in black and white ovals, which indicates the superiority of the proposed method over Hansen's product. On the other hand, almost all of the disturbed areas during 2016-2019 in Hansen's product can be found in the corresponding areas of the result shown in Figure 11(b). This is because the Landsat images used in Hansen's product were also applied in the proposed method. Moreover, besides the Landsat-7/8 images, Sentinel-2 images were also used in the proposed method to detect more disturbed areas within a short period. Although Hansen's product is limited for tracking small-scale forest disturbances, it may have a

high accuracy for the detection of large-scale (e.g., more than 100 ha) forest disturbances. This is because large-scale forest disturbance may need a long time (e.g., one year) to recover, and the spatial and temporal resolutions of the Landsat images used in Hansen's product can meet this requirement. Therefore, in future research, it is of high interest to combine Hansen's product with the proposed method to provide a full estimation of both large- and small-scale tropical forest disturbances.

5.4 Limitations and future research

From the results of the above two data evaluations and comparisons, it is evident that both the temporal and spatial resolutions of image data sets are critical variables in the monitoring of small areas of disturbance in tropical forests. The spatial and temporal scales of relevance depend on the processes operating on the landscape. For small area forest disturbances (e.g., <1 ha), such as those arising from selective logging and smallholder clearing, there is usually no long-term land cover conversion for the disturbed area, which will typically be covered by vegetation within a year, and make the forest disturbance signal disappear in a short time. It is, therefore, important that the satellite sensor images used in monitoring have both a fine spatial and temporal resolution. Here, the temporal resolution was enhanced by utilizing both Landsat and Sentinel-2 data and the spatial resolution of the Landsat imagery enhanced by a super-resolution analysis. In this way, more disturbed areas could be found using the proposed method. Specifically, a deep learning-based downscaling method was used to increase the spatial resolution of Landsat *r*NBR images to that of Sentinel-2 images, and it performed better than the traditional spatial interpolation approach in the above two experiments. Deep learning has been shown to be a promising approach for remote sensing (Zhu et al. 2017; Ma et al. 2019), but there are few studies addressing forest disturbance with deep learning approaches. Emerging image super-resolution methods may be superior to the CNN-VDSR used in this paper, such as super-resolution using convolution neural network (SRCNN) (Dong et al. 2016), efficient sub-Pixel convolutional neural network (ESPCN) (Shi et al. 2016), deeply recursive convolutional network (DRCN) (Kim et al. 2016b), information distillation network (IDN) (Hui et al. 2018), and enhanced super-resolution generative adversarial nets (ESRGAN) (Wang et al. 2019), can also be applied to increase the spatial resolution of Landsat *r*NBR images (Wang et al. 2020). We set this as an open issue, and any other useful spatial downscaling methods, including deep learning approaches or traditional spatial interpolation approaches, can be applied to fill the spatial resolution gap between the Landsat and Sentinel-2 images. As shown in Figure 8, the threshold value δ

has a key impact on the production of the final forest disturbance map, and the value is suggested to be set in the range of 0.14-0.16. However, the suggested threshold value range may not hold true in other areas outside of the study area. That is, it is not clear how robust the threshold range is to different contexts. Therefore, in future research, the threshold should be evaluated for other tropical forest areas.

6. Conclusion

Landsat imagery has been used widely to study forest disturbance. The potential of Landsat is, however, limited in tropical regions by cloud cover. Moreover, in some tropical regions key disturbance events are very small and these may not be detected reliably because of the relatively coarse spatial resolution of Landsat sensors. Here, we combine Landsat and Sentinel-2 data to generate a denser temporal series of images to reduce the effects of cloud and also rescale the Landsat images to the finer Sentinel-2 resolution. Based on the self-referencing NBR vegetation index and a deep learning-based downscaling method, all available Landsat-7/8 and Sentinel-2 images during 2016-2019 were fused to produce a forest disturbance map. The fused time-series of images yielded the most accurate forest disturbance map. Critically, the fused Sentinel-2 and Landsat fine-resolution *r*NBR imagery produced results where OA increased by between 1.84% and 10.77%, and allowed 11% to 21% more disturbed areas to be detected than was possible using the Sentinel-2 or Landsat-7/8 images alone. Meanwhile, by using the mean values of the fused annual fine-resolution *r*NBR images, we found that 1.42% of the total forest disturbance areas during 2016-2019 experienced multiple forest disturbances. In future research, it is of great interest to explore the potential of alternative deep learning-based image downscaling methods to produce the fine-resolution Landsat *r*NBR images and to evaluate and improve effectiveness and extensiveness of the proposed method in other tropical forest areas.

Acknowledgments

The authors wish to thank Dr. Andreas Langner from European Commission for providing the free Forest Canopy Disturbance Monitoring (FCDM, https://zenodo.org/record/3240021) tool, and also thank the Google Earth for providing the VHR images used in this study. This work was supported by the Key Research Program of Frontier Sciences, Chinese Academy of Sciences (ZDBS-LY-DQC034), National Natural Science Foundation of China (41801292), Hubei Provincial Natural Science Foundation for Innovation Groups (2019CFA019), the Strategic Priority Research Program of Chinese Academy of Sciences (XDA2003030201), Hubei Province Natural Science Fund for Distinguished Young Scholars

(2018CFA062), Hubei Provincial Natural Science Foundation (2018CFB274).

References

Asner, G., Knapp, D., Balaji, A., & Paez-Acosta, G., 2009. Automated mapping of tropical deforestation and forest degradation: CLASlite. J. Appl. Remote. Sens., 3, 033543, https://doi.org/10.1117/1.3223675

Baccini, A., Walker, W., Carvalho, L., Farina, M., Sulla-Menashe, D., & Houghton, R.A., 2017. Tropical forests are a net carbon source based on aboveground measurements of gain and loss. Science, 358, 230-234, https://doi.org/10.1126/science.aam5962

Banskota, A., Kayastha, N., Falkowski, M.J., Wulder, M.A., Froese, R.E., & White, J.C., 2014. Forest Monitoring Using Landsat Time Series Data: A Review. Can. J. Remote. Sens., 40, 362-384, https://doi.org/10.1080/07038992.2014.987376

Barlow, J., Lennox, G.D., Ferreira, J., Berenguer, E., Lees, A.C., Nally, R.M., et al., 2016. Anthropogenic disturbance in tropical forests can double biodiversity loss from deforestation. Nature, 535, 144-147, https://doi.org/10.1038/nature18326

Bullock, E.L., Woodcock, C.E., & Olofsson, P., 2020. Monitoring tropical forest degradation using spectral unmixing and Landsat time series analysis. Remote Sens. Environ., 238, 110968, https://doi.org/10.1016/j.rse.2018.11.011

Claverie, M., Ju, J., Masek, J.G., Dungan, J.L., Vermote, E.F., Roger, J.-C., et al., 2018. The Harmonized Landsat and Sentinel-2 surface reflectance data set. Remote Sens. Environ., 219, 145-161, https://doi.org/10.1016/j.rse.2018.09.002

Cohen, W.B., Spies, T.A., Alig, R.J., Oetter, D.R., Maiersperger, T.K., & Fiorella, M., 2002. Characterizing 23 Years (1972–95) of Stand Replacement Disturbance in Western Oregon Forests with Landsat Imagery. Ecosystems, 5, 122-137, https://doi.org/10.1007/s10021-001-0060-X

Curtis, P.G., Slay, C.M., Harris, N.L., Alexandra, T., & Hansen, M.C., 2018. Classifying drivers of global forest loss. Science, 316, 1108-1111, https://doi.org/10.1126/science.aau3445

Dong, C., Loy, C.C., He, K., & Tang, X., 2016. Image Super-Resolution Using Deep Convolutional Networks. IEEE Trans. Pattern Anal. Mach. Intell., 38, 295-307, https://doi.org/10.1109/TPAMI.2015.2439281

Dong, J., Xiao, X., Sheldon, S., Biradar, C., Duong, N.D., & Hazarika, M., 2012a. A comparison of forest cover maps in Mainland Southeast Asia from multiple sources: PALSAR, MERIS, MODIS and FRA. Remote Sens. Environ., 127, 60-73, https://doi.org/10.1016/j.rse.2012.08.022

Dong, J., Xiao, X., Sheldon, S., Biradar, C., & Xie, G., 2012b. Mapping tropical forests and rubber plantations in complex landscapes by integrating PALSAR and MODIS imagery. ISPRS-J. Photogramm. Remote Sens., 74, 20-33, https://doi.org/10.1016/j.isprsjprs.2012.07.004

Du, Y., Zhang, Y., Ling, F., Wang, Q., Li, W., & Li, X., 2016. Water Bodies' Mapping from Sentinel-2 Imagery with Modified Normalized Difference Water Index at 10-m Spatial Resolution Produced by Sharpening the SWIR Band. Remote Sens., 8, 354, https://doi.org/10.3390/rs8040354

Frolking, S., Palace, M.W., Clark, D.B., Chambers, J.Q., Shugart, H.H., & Hurtt, G.C., 2009. Forest disturbance and recovery: A general review in the context of spaceborne remote sensing of impacts on aboveground biomass and canopy structure. J. Geophys. Res. Biogeosci., 114https://doi.org/10.1029/2008jg000911

Garzelli, A., & Nencini, F., 2009. Hypercomplex Quality Assessment of Multi/Hyperspectral Images. IEEE Geosci. Remote Sens. Lett., 6, 662-665, https://doi.org/10.1109/LGRS.2009.2022650

744 Ge, Y., Jin, Y., Stein, A., Chen, Y., Wang, J., Wang, J., et al., 2019. Principles and methods of scaling
745 geospatial Earth science data. Earth-Sci. Rev., 197, 102897,
746 https://doi.org/10.1016/j.earscirev.2019.102897
747 Hansen, M.C., Potapov, P.V., Moore, R., Hancher, M., Turubanova, S.A., Tyukavina, A., et al., 2013.
748 High-Resolution Global Maps of 21st-Century Forest Cover Change. Science, 342, 850-853,
749 https://doi.org/10.1126/science.1244693
750 Harris, N.L., Goldman, E., Gabris, C., Nordling, J., Minnemeyer, S., Ansari, S., et al., 2017. Using spatial
751 statistics to identify emerging hot spots of forest loss. Environ. Res. Lett., 12, 024012,
752 https://doi.org/10.1088/1748-9326/aa5a2f
753 Hermosilla, T., Wulder, M.A., White, J.C., Coops, N.C., & Hobart, G.W., 2015. Regional detection,
754 characterization, and attribution of annual forest change from 1984 to 2012 using Landsat-derived
755 time-series metrics. Remote Sens. Environ., 170, 121-132,
756 https://doi.org/10.1016/j.rse.2015.09.004
757 Hermosilla, T., Wulder, M.A., White, J.C., Coops, N.C., Hobart, G.W., & Campbell, L.B., 2016. Mass
758 data processing of time series Landsat imagery: pixels to data products for forest monitoring. Int. J.
759 Digit. Earth, 9, 1035-1054, https://doi.org/10.1080/17538947.2016.1187673
760 Hirschmugl, M., Deutscher, J., Gutjahr, K., Sobe, C., & Schardt, M., 2017. Combined use of SAR and
761 optical time series data for near real-time forest disturbance mapping. 2017 9th International
762 Workshop on the Analysis of Multitemporal Remote Sensing Images (MultiTemp), 1-4,
763 https://doi.org/10.1109/Multi-Temp.2017.8035208
764 Huang, C., Goward, S.N., Masek, J.G., Thomas, N., Zhu, Z., & Vogelmann, J.E., 2010. An automated
765 approach for reconstructing recent forest disturbance history using dense Landsat time series stacks.
766 Remote Sens. Environ., 114, 183-198, https://doi.org/10.1016/j.rse.2009.08.017
767 Huang, C., Kim, S., Altstatt, A., Townshend, J.R.G., Davis, P., Song, K., et al., 2007. Rapid loss of
768 Paraguay's Atlantic forest and the status of protected areas — A Landsat assessment. Remote Sens.
769 Environ., 106, 460-466, https://doi.org/10.1016/j.rse.2006.09.016
770 Hui, Z., Wang, X., & Gao, X., 2018. Fast and Accurate Single Image Super-Resolution via Information
771 Distillation Network. 2018 IEEE/CVF Conference on Computer Vision and Pattern Recognition,
772 723-731, https://doi.org/10.1109/CVPR.2018.00082
773 Jackson, B., Sparks, J., Brown, C., & Boyd, D., 2020. Understanding the co-occurrence of tree loss and
774 modern slavery to improve efficacy of conservation actions and policies. Conservation Science and
775 Practice, 2, 1-13, https://doi.org/10.1111/csp2.183
776 Jarihani, B., McVicar, T., Van Niel, T., Emelyanova, I., Callow, J., & Johansen, K., 2014. Blending
777 Landsat and MODIS Data to Generate Multispectral Indices: A Comparison of "Index-then-Blend"
778 and "Blend-then-Index" Approaches. Remote Sens., 6, 9213-9238,
779 https://doi.org/10.3390/rs6109213
780 Ju, J., & Roy, D.P., 2008. The availability of cloud-free Landsat ETM+ data over the conterminous United
781 States and globally. Remote Sens. Environ., 112, 1196-1211,
782 https://doi.org/10.1016/j.rse.2007.08.011
783 Kalamandeen, M., Gloor, E., Mitchard, E., Quincey, D., Ziv, G., Spracklen, D., et al., 2018. Pervasive
784 Rise of Small-scale Deforestation in Amazonia. Scientific Reports, 8, 1600,
785 https://doi.org/10.1038/s41598-018-19358-2
786 Kennedy, R.E., Cohen, W.B., & Schroeder, T.A., 2007. Trajectory-based change detection for automated
787 characterization of forest disturbance dynamics. Remote Sens. Environ., 110, 370-386,

https://doi.org/10.1016/j.rse.2007.03.010
Kennedy, R.E., Yang, Z., & Cohen, W.B., 2010. Detecting trends in forest disturbance and recovery using yearly Landsat time series: 1. LandTrendr — Temporal segmentation algorithms. Remote Sens. Environ., 114, 2897-2910, https://doi.org/10.1016/j.rse.2010.07.008
Kim, D.-H., Sexton, J.O., Noojipady, P., Huang, C., Anand, A., Channan, S., et al., 2014. Global, Landsat-based forest-cover change from 1990 to 2000. Remote Sens. Environ., 155, 178-193, https://doi.org/10.1016/j.rse.2014.08.017
Kim, J., Lee, J.K., & Lee, K.M., 2016a. Accurate Image Super-Resolution Using Very Deep Convolutional Networks. 2016 IEEE Conference on Computer Vision and Pattern Recognition (CVPR), 1646-1654, https://doi.org/10.1109/Cvpr.2016.182
Kim, J., Lee, J.K., & Lee, K.M., 2016b. Deeply-Recursive Convolutional Network for Image Super-Resolution. 2016 IEEE Conference on Computer Vision and Pattern Recognition (CVPR), 1637-1645, https://doi.org/10.1109/CVPR.2016.181
Kleinschroth, F., Healey, J.R., Sist, P., Mortier, F., & Gourlet-Fleury, S., 2016. How persistent are the impacts of logging roads on Central African forest vegetation? J. Appl. Ecol., 53, 1127-1137, https://doi.org/10.1111/1365-2664.12661
Kleinschroth, F., Laporte, N., Laurance, W.F., Goetz, S.J., & Ghazoul, J., 2019. Road expansion and persistence in forests of the Congo Basin. Nat. Sustain., 2, 628-634, https://doi.org/10.1038/s41893-019-0310-6
Langner, A., Miettinen, J., Kukkonen, M., Vancutsem, C., Simonetti, D., Vieilledent, G., et al., 2018. Towards Operational Monitoring of Forest Canopy Disturbance in Evergreen Rain Forests: A Test Case in Continental Southeast Asia. Remote Sens., 10, 544, https://doi.org/10.3390/rs10040544
Lima, T.A., Beuchle, R., Langner, A., Grecchi, R.C., Griess, V.C., & Achard, F., 2019. Comparing Sentinel-2 MSI and Landsat 8 OLI Imagery for Monitoring Selective Logging in the Brazilian Amazon. Remote Sens., 11https://doi.org/10.3390/rs11080961
Ling, F., Boyd, D., Ge, Y., Foody, G.M., Li, X., Wang, L., et al., 2019. Measuring River Wetted Width From Remotely Sensed Imagery at the Subpixel Scale With a Deep Convolutional Neural Network. Water Resour. Res., 55, 5631-5649, https://doi.org/10.1029/2018wr024136
Ling, F., & Foody, G.M., 2019. Super-resolution land cover mapping by deep learning. Remote Sens. Lett., 10, 598-606, https://doi.org/10.1080/2150704X.2019.1587196
Lu, D., Mausel, P., Brondízio, E., & Moran, E., 2004. Change detection techniques. Int. J. Remote Sens., 25, 2365-2401, https://doi.org/10.1080/0143116031000139863
Ma, L., Liu, Y., Zhang, X., Ye, Y., Yin, G., & Johnson, B.A., 2019. Deep learning in remote sensing applications: A meta-analysis and review. ISPRS-J. Photogramm. Remote Sens., 152, 166-177, https://doi.org/10.1016/j.isprsjprs.2019.04.015
Masek, J.G., Huang, C., Wolfe, R., Cohen, W., Hall, F., Kutler, J., et al., 2008. North American forest disturbance mapped from a decadal Landsat record. Remote Sens. Environ., 112, 2914-2926, https://doi.org/10.1016/j.rse.2008.02.010
Olofsson, P., Foody, G.M., Herold, M., Stehman, S.V., Woodcock, C.E., & Wulder, M.A., 2014. Good practices for estimating area and assessing accuracy of land change. Remote Sens. Environ., 148, 42-57, https://doi.org/10.1016/j.rse.2014.02.015
Pan, Y., Birdsey, R.A., Fang, J., Houghton, R., Kauppi, P.E., Kurz, W.A., et al., 2011. A large and persistent carbon sink in the World's forests. Science, 333, 988-993, https://doi.org/10.1126/science.1201609

Potapov, P.V., Turubanova, S.A., Hansen, M.C., Adusei, B., Broich, M., Altstatt, A., et al., 2012. Quantifying forest cover loss in Democratic Republic of the Congo, 2000–2010, with Landsat ETM+ data. Remote Sens. Environ., 122, 106-116, https://doi.org/10.1016/j.rse.2011.08.027

Pouliot, D., Latifovic, R., Pasher, J., & Duffe, J., 2018. Landsat Super-Resolution Enhancement Using Convolution Neural Networks and Sentinel-2 for Training. Remote Sens., 10, 394, https://doi.org10.3390/rs10030394

Qin, Y., Xiao, X., Dong, J., Zhang, Y., Wu, X., Shimabukuro, Y., et al., 2019. Improved estimates of forest cover and loss in the Brazilian Amazon in 2000–2017. Nat. Sustain., 2, 764-772, https://doi.org/10.1038/s41893-019-0336-9

Qiu, S., Zhu, Z., & He, B., 2019. Fmask 4.0: Improved cloud and cloud shadow detection in Landsats 4–8 and Sentinel-2 imagery. Remote Sens. Environ., 231, 111205, https://doi.org/10.1016/j.rse.2019.05.024

Saatchi, S.S., Harris, N.L., Brown, S., Lefsky, M., Mitchard, E.T.A., Salas, W., et al., 2011. Benchmark map of forest carbon stocks in tropical regions across three continents. Proceedings of the National Academy of Sciences, 108, 9899-9904, https://doi.org10.1073/pnas.1019576108

Sexton, J.O., Song, X.-P., Feng, M., Noojipady, P., Anand, A., Huang, C., et al., 2013. Global, 30-m resolution continuous fields of tree cover: Landsat-based rescaling of MODIS vegetation continuous fields with lidar-based estimates of error. Int. J. Digit. Earth, 6, 427-448, https://doi.org10.1080/17538947.2013.786146

Shao, Z., Cai, J., Fu, P., Hu, L., & Liu, T., 2019. Deep learning-based fusion of Landsat-8 and Sentinel-2 images for a harmonized surface reflectance product. Remote Sens. Environ., 235, 111425, https://doi.org/10.1016/j.rse.2019.111425

Shi, W., Caballero, J., Huszár, F., Totz, J., Aitken, A.P., Bishop, R., et al., 2016. Real-Time Single Image and Video Super-Resolution Using an Efficient Sub-Pixel Convolutional Neural Network. 2016 IEEE Conference on Computer Vision and Pattern Recognition (CVPR), 1874-1883, https://doi.org/10.1109/CVPR.2016.207

Souza, C.M., Roberts, D.A., & Cochrane, M.A., 2005. Combining spectral and spatial information to map canopy damage from selective logging and forest fires. Remote Sens. Environ., 98, 329-343, https://doi.org/10.1016/j.rse.2005.07.013

Souza, J., Carlos M., Siqueira, J.V., Sales, M.H., Fonseca, A.V., Ribeiro, J.G., Numata, I., et al., 2013. Ten-Year Landsat Classification of Deforestation and Forest Degradation in the Brazilian Amazon. Remote Sens., 5, 5493-5513, https://doi.org/10.3390/rs5115493

Tang, X., Bullock, E.L., Olofsson, P., Estel, S., & Woodcock, C.E., 2019. Near real-time monitoring of tropical forest disturbance: New algorithms and assessment framework. Remote Sens. Environ., 224, 202-218, https://doi.org/10.1016/j.rse.2019.02.003

Townshend, J.R., Masek, J.G., Huang, C., Vermote, E.F., Gao, F., Channan, S., et al., 2012. Global characterization and monitoring of forest cover using Landsat data: opportunities and challenges. Int. J. Digit. Earth, 5, 373-397, https://doi.org/10.1080/17538947.2012.713190

Tyukavina, A., Hansen, M.C., Potapov, P., Parker, D., Okpa, C., Stehman, S.V., et al., 2018. Congo Basin forest loss dominated by increasing smallholder clearing. Sci. Adv., 4, 1-12, https://doi.org/10.1126/sciadv.aat2993

Uriarte, M., Canham, C.D., Thompson, J., Zimmerman, J.K., Murphy, L., Sabat, A.M., et al., 2009. Natural disturbance and human land use as determinants of tropical forest dynamics: results from a forest simulator. Ecol. Monogr., 79, 423-443, https://doi.org/10.1890/08-0707.1

Vaglio Laurin, G., Puletti, N., Hawthorne, W., Liesenberg, V., Corona, P., Papale, D., et al., 2016. Discrimination of tropical forest types, dominant species, and mapping of functional guilds by hyperspectral and simulated multispectral Sentinel-2 data. Remote Sens. Environ., 176, 163-176, https://doi.org/10.1016/j.rse.2016.01.017

Verbesselt, J., Zeileis, A., & Herold, M., 2012. Near real-time disturbance detection using satellite image time series. Remote Sens. Environ., 123, 98-108, https://doi.org/10.1016/j.rse.2012.02.022

Wang, Q., Blackburn, G.A., Onojeghuo, A.O., Dash, J., Zhou, L., Zhang, Y., et al., 2017. Fusion of Landsat 8 OLI and Sentinel-2 MSI Data. IEEE Trans. Geosci. Remote Sens., 55, 3885-3899, https://doi.org/10.1109/TGRS.2017.2683444

Wang, X., Yu, K., Wu, S., Gu, J., Liu, Y., Dong, C., et al., 2019. ESRGAN: Enhanced Super-Resolution Generative Adversarial Networks. Computer Vision – ECCV 2018 Workshops, 63-79, https://doi.org/10.1007/978-3-030-11021-5_5

Wang, Z., Chen, J., & Hoi, S.C.H., 2020. Deep Learning for Image Super-resolution: A Survey. IEEE Trans. Pattern Anal. Mach. Intell., 1-1, https://doi.org/10.1109/TPAMI.2020.2982166

White, J.C., Wulder, M.A., Hermosilla, T., Coops, N.C., & Hobart, G.W., 2017. A nationwide annual characterization of 25years of forest disturbance and recovery for Canada using Landsat time series. Remote Sens. Environ., 194, 303-321, https://doi.org/10.1016/j.rse.2017.03.035

Zhang, Q., Devers, D., Desch, A., Justice, C.O., & Townshend, J., 2005. Mapping tropical deforestation in Central Africa. Environ. Monit. Assess., 101, 69-83, https://doi.org/10.1007/s10661-005-9132-2

Zhang, Y., Ling, F., Foody, G.M., Ge, Y., Boyd, D.S., Li, X., et al., 2019. Mapping annual forest cover by fusing PALSAR/PALSAR-2 and MODIS NDVI during 2007–2016. Remote Sens. Environ., 224, 74-91, https://doi.org/10.1016/j.rse.2019.01.038

Zhu, X.X., Tuia, D., Mou, L., Xia, G., Zhang, L., Xu, F., et al., 2017. Deep Learning in Remote Sensing: A Comprehensive Review and List of Resources. IEEE Trans. Geosci. Remote Sens., 5, 8-36, https://doi.org/10.1109/MGRS.2017.2762307

Zhu, Z., Woodcock, C.E., & Olofsson, P., 2012. Continuous monitoring of forest disturbance using all available Landsat imagery. Remote Sens. Environ., 122, 75-91, https://doi.org/10.1016/j.rse.2011.10.030